Electronic Supplementary Material (ESI) for Journal of Materials Chemistry C.

Electronic Supplementary Information

for

A Possibly Highly Conducting State in an Optically Excited Molecular Crystal

Toshio Naito [1,2,3,*], Tomoaki Karasudani [1], Ryoma Yamamoto [1], Ming Yang Zhang [1], and Takashi Yamamoto [1,3,4]

[1] Graduate School of Science and Engineering, Ehime University, Matsuyama 790-8577, Japan

[2] Advanced Research Support Center (ADRES), Ehime University, Matsuyama 790-8577, Japan

[3] Research Unit for Development of Organic Superconductors, Ehime University, Matsuyama 790-8577, Japan

[4] Research Unit for Materials Science under Ultra-high Pressure, Ehime University, Matsuyama 790-8577, Japan

* Author to whom correspondence should be addressed; E-Mail: tnaito@ehime-u.ac.jp;
Tel.: +81-89-927-9604; Fax: +81-89-927-9604.

Contents

§1. X-ray structural analyses

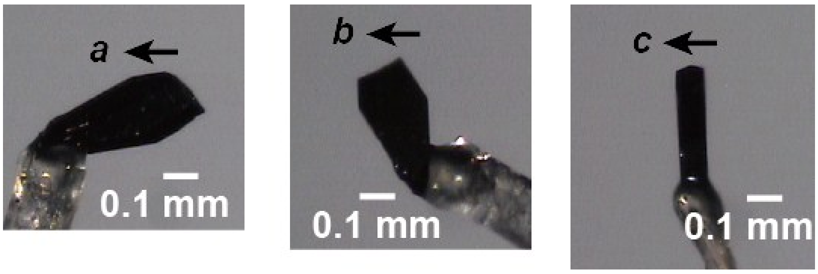

Figure S1. Single crystal of BPY[Ni(dmit)$_2$]$_6$· 3CH$_3$CN, **1**. A different crystal from that shown in Fig. 1A.

The crystals of **1** were elongated platelets with the long axis nearly along the *a*-axis. The summary of X-ray structural analysis is shown in **Table S1**. Crystallographic data have been deposited with Cambridge Crystallographic Data Centre. Also shown are the oscillation photographs taken at 298 K and 80 K around the $[3\bar{1}0]$ direction, showing that the superstructure does not change between these temperatures.

Table S1. Summary of X-ray structural analysis.

Formula	$C_{54}H_{21}N_5Ni_6S_{60}$	
M (g mol^{-1})	3015.59	
Temperature (K)	296	100
Crystal system	Triclinic	
Space Group	$P\bar{1}$ (#2)	
a (Å)	13.4930(3)	13.2763(2)
b (Å)	18.9594(4)	18.8083(3)
c (Å)	19.9690(4)	19.8878(4)
α (°)	94.380(7)	94.427(7)
β (°)	99.819(7)	99.435(7)
γ (°)	91.961(7)	91.988(7)
V (Å^3)	5013.1(2)	4878.61(19)
Z	2	
D_{calc} (g cm^{-3})	1.998	2.053
μ (Cu $K\alpha$) (cm^{-1})	13.256	13.622
CCDC deposit #	1558401	1816550
Reflection/Parameter	15.90	15.42
Max peak (e$^-$/Å^3)	1.39	0.81
Min peak (e$^-$/Å^3)	-0.75	-1.10
R_1, wR_2	0.0675 ^{1}, 0.1745 ^{2}	0.0566 ^{1}, 0.1515 ^{2}
Goodness of Fit	0.757	0.659
Max Shift/Error	0.000	0.001

^{1} $I > 2.00\sigma(I)$. ^{2} All reflections.

Table S1(continued). Summary of X-ray structural analysis.

Formula	$C_{54}H_{21}N_5Ni_6S_{60}$			
M (g mol^{-1})	3015.59			
Temperature (K)	296	296	298	298
Conditions[3]	Before UV irradiation	After UV irradiation	Before high pressure (8 kbar)	After high pressure (8 kbar)
Crystal system	Triclinic			
Space Group	$P\bar{1}$ (#2)			
a (Å)	13.4901(3)	13.492(3)	13.4967(5)	13.5177(6)
b (Å)	18.9607(4)	18.967(4)	18.9687(5)	18.9535(7)
c (Å)	19.9538(4)	19.970(5)	19.9725(5)	19.9913(7)
α (°)	94.2960(17)	94.376(4)	94.536(2)	94.334(3)
β (°)	99.8200(16)	99.789(4)	99.859(2)	99.919(3)
γ (°)	92.0500(17)	91.960(4)	92.004(2)	91.960(3)
V (Å^3)	5008.78(19)	5015.4(19)	5015.8(3)	5025.1(3)
Z	2			
D_{calc} (g cm^{-3})	1.999	1.997	1.997	1.993
μ (Mo $K\alpha$) (cm^{-1})	23.984	23.953	23.951	23.906
Reflection/Parameter	20.27	24.00	25.04	25.06
Max peak (e$^-$/Å^3)	0.63	1.68	0.88	0.65
Min peak (e$^-$/Å^3)	-0.59	-0.92	-0.80	-0.57
R_1, wR_2	0.0354 [1], 0.0909 [2]	0.0631 [1], 0.1682 [2]	0.0528 [1], 0.1594 [2]	0.0504 [1], 0.1310 [2]
Goodness of Fit	1.017	0.964	1.024	1.019
Max Shift/Error	0.002	0.001	0.001	0.002

[1] $I > 2.00\sigma(I)$. [2] All reflections. [3] The same samples were used in the examination of effect of UV irradiation and high pressure, respectively. UV irradiation was carried out at 93 K, while high pressure (8 kbar) was applied at 296 K.

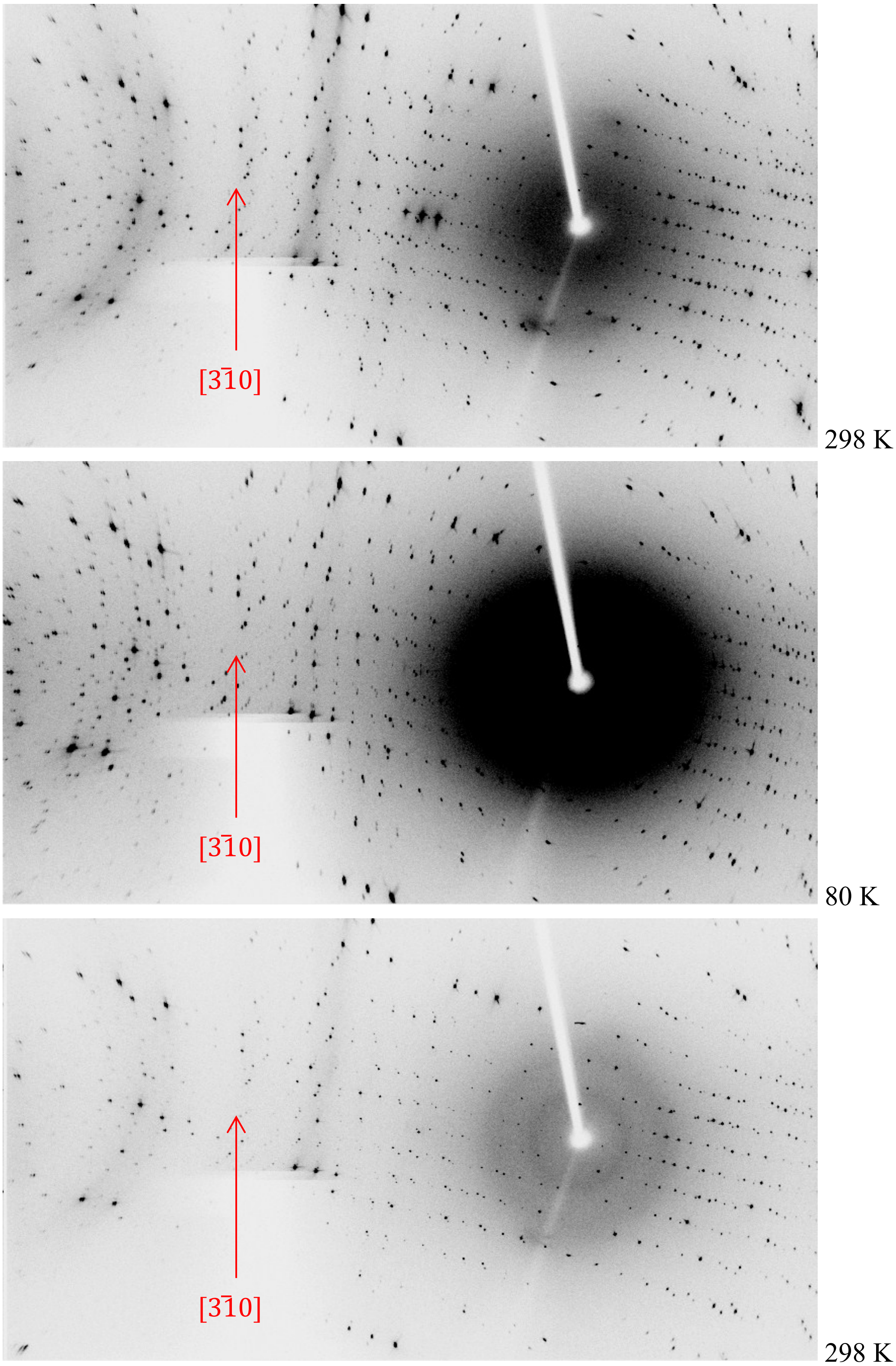

Figure S2. X-ray oscillation photographs of BPY[Ni(dmit)$_2$]$_6$· 3CH$_3$CN, **1**.
Taken for the same single crystal in the order of 298 K(upper), 80 K(middle), and 298 K(lower), again. Note that no diffuse scatterings or satellites are observed in the [3$\bar{1}$0] direction.

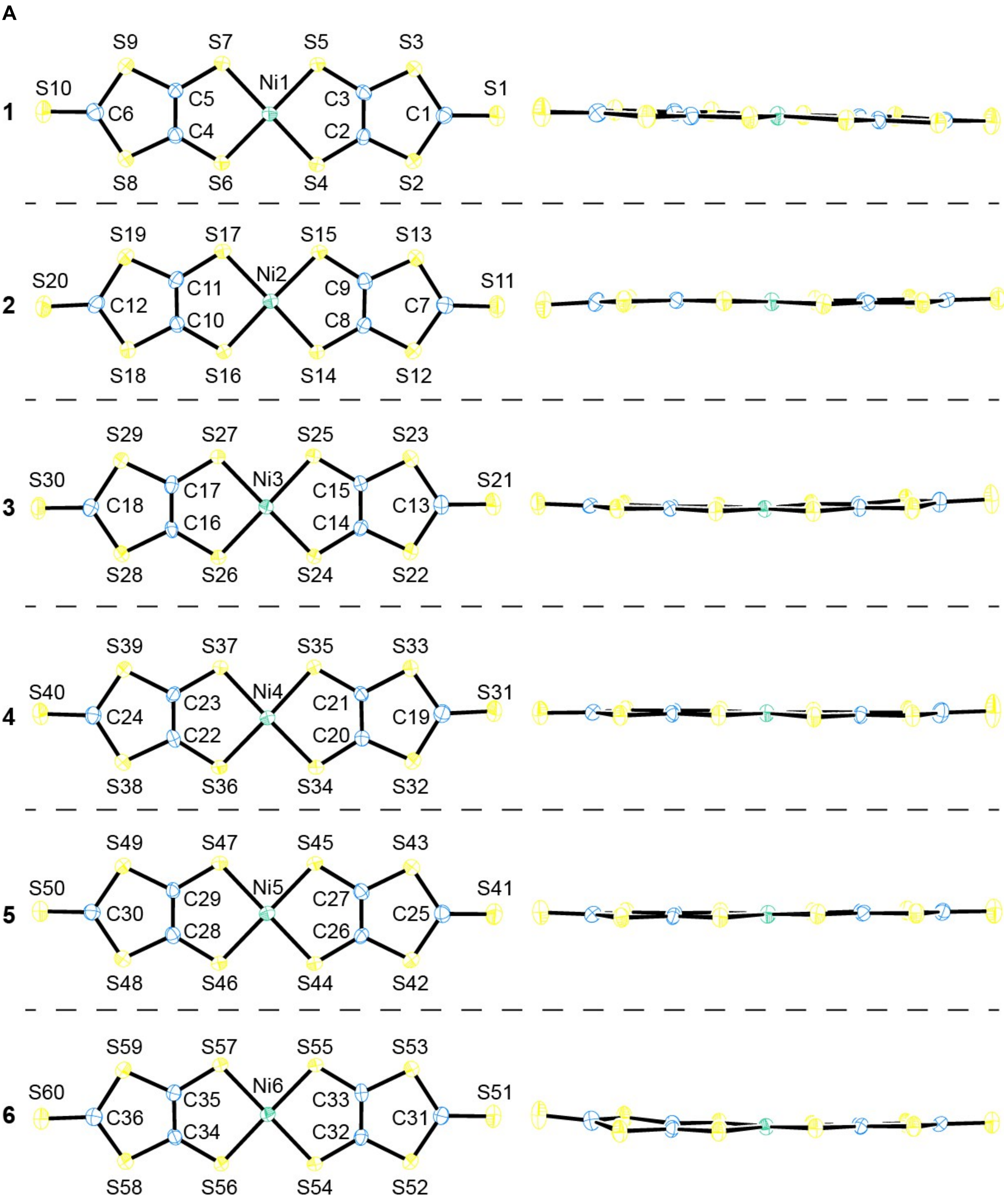

Figure S3.

(**A**) Six kinds of crystallographically independent Ni(dmit)$_2$ anions in BPY[Ni(dmit)$_2$]$_6$·3CH$_3$CN (observed at 296 K). Front (left) and side (right) views. Yellow, green, and blue spheres indicate S, Ni, and C atoms, respectively. The numbers (**1**–**6**) correspond to those in **Figure 1**. The molecular structures remain essentially the same at 100 K.

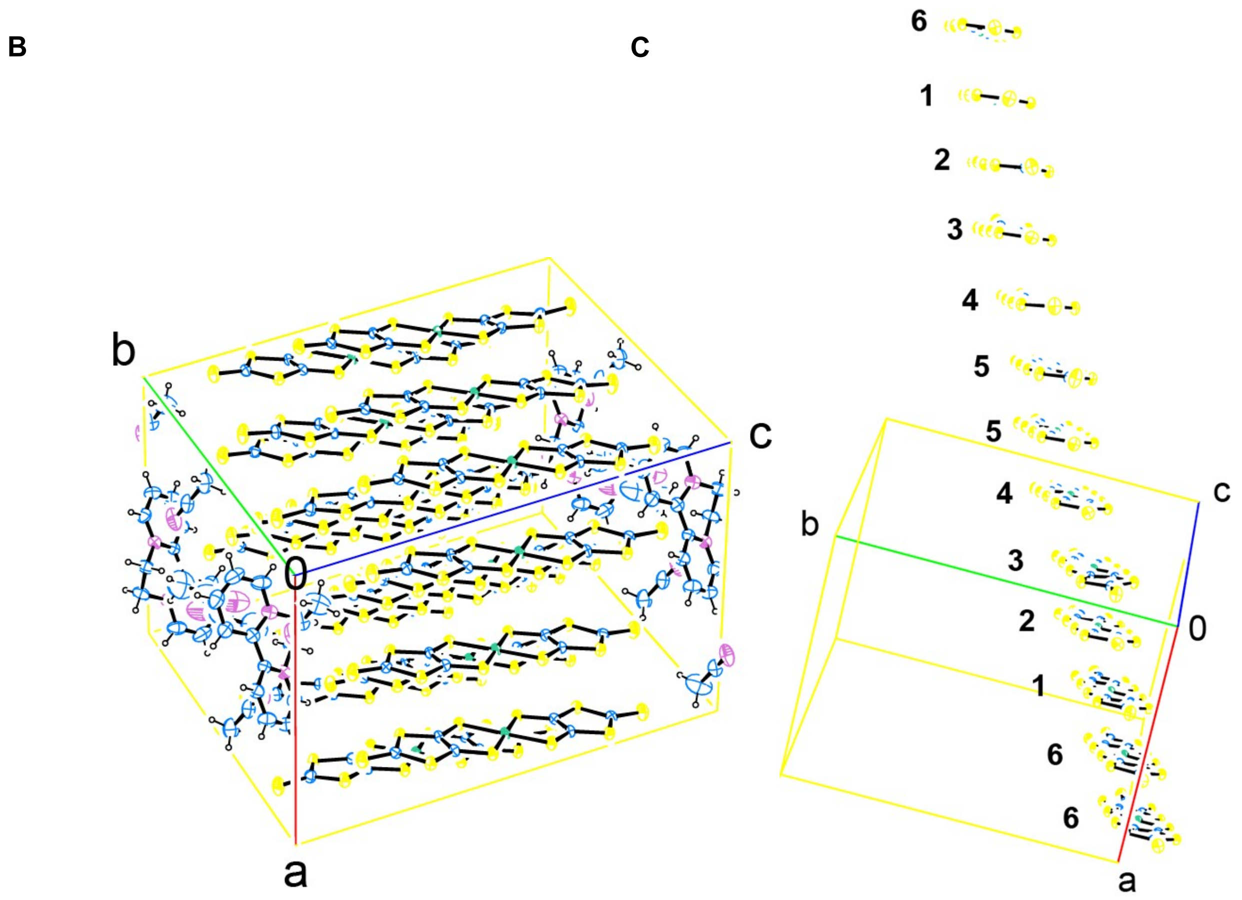

Figure S3 (continued).

(**B**) Overview of the molecular arrangement in BPY[Ni(dmit)$_2$]$_6$·3CH$_3$CN (observed at 296 K).
(**C**) Ni(dmit)$_2$ stacking column approximately along the $[3\bar{1}0]$ direction. Open, yellow, green, and blue spheres designate H, S, Ni, and C atoms, respectively. The numbers (**1**–**6**) correspond to those in **Figure 1**. For the molecular arrangement between adjacent columns, see **Figures S6** and **S7**. The crystal structures remain essentially the same at 100 K.

§2. Electrical resistivity (dark)

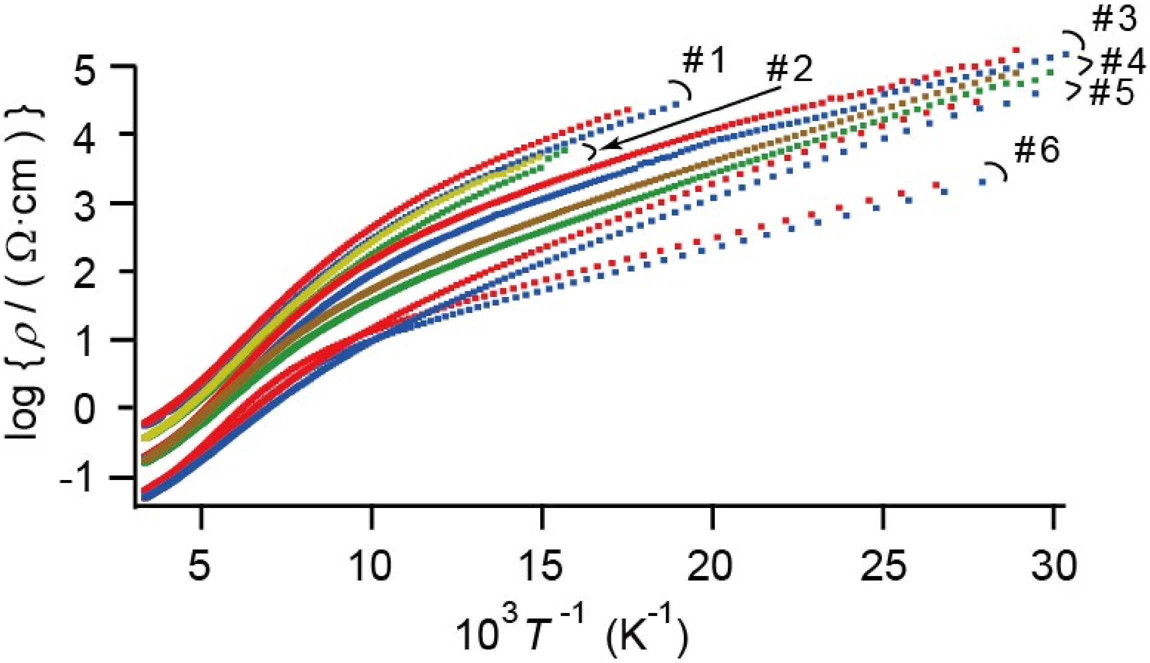

Figure S4.

Sample dependence of the resistivity behavior. Logarithm of the electrical resistivity of BPY[Ni(dmit)$_2$]$_6$·3CH$_3$CN *vs*. the inverse temperature. These measurements are from different samples than that used to obtain the data in **Figure 2B**. The different specimens are designated as #1–6, showing that they share qualitative behavior.

§3. Theoretical calculations

Calculations of electronic band structures and related properties

Based on the atomic parameters obtained from the X-ray structural analysis at 296 K, an extended Hückel tight-binding band structure calculation was carried out using CAESAR ver. 1.0 and 2.0 (PrimeColor Software, Inc.) as described in previous papers.[S1,S2] The similar calculation using the atomic parameters at 100 K gave almost identical results with those shown here. Overlap and transfer integrals between the singly occupied molecular orbitals of Ni(dmit)$_2$ were also calculated using the same software. The atomic orbital parameters and Slater-type orbital (STO) basis sets assumed in the calculation are tabulated in **Tables S2**. Calculation results using empirical methods are generally dependent on the parameters used. Additionally, the crystal structure and electrical behavior of BPY[Ni(dmit)$_2$]$_6$·3CH$_3$CN suggests that the calculated band structure is sensitive to the chosen parameters, i.e., the basis set selected. Therefore, we examined different patterns for the band calculation using different parameter sets to compare the results. A basis set called “CRMM” (**Table S2A**) gave a non-metallic band structure (**Figure S5A**), while another basis set called “Collected” (**Table S2B**) gave a metallic band structure (**Figure S5B**). Considering the observed non-metallic behavior, the non-metallic band structure was accepted. The calculation results from the other parameter set (“Collected;” **Table S2B**) are also shown below (**Figure S5B**) to demonstrate the sensitivity of the results to the parameters in the case of this molecular system.

A

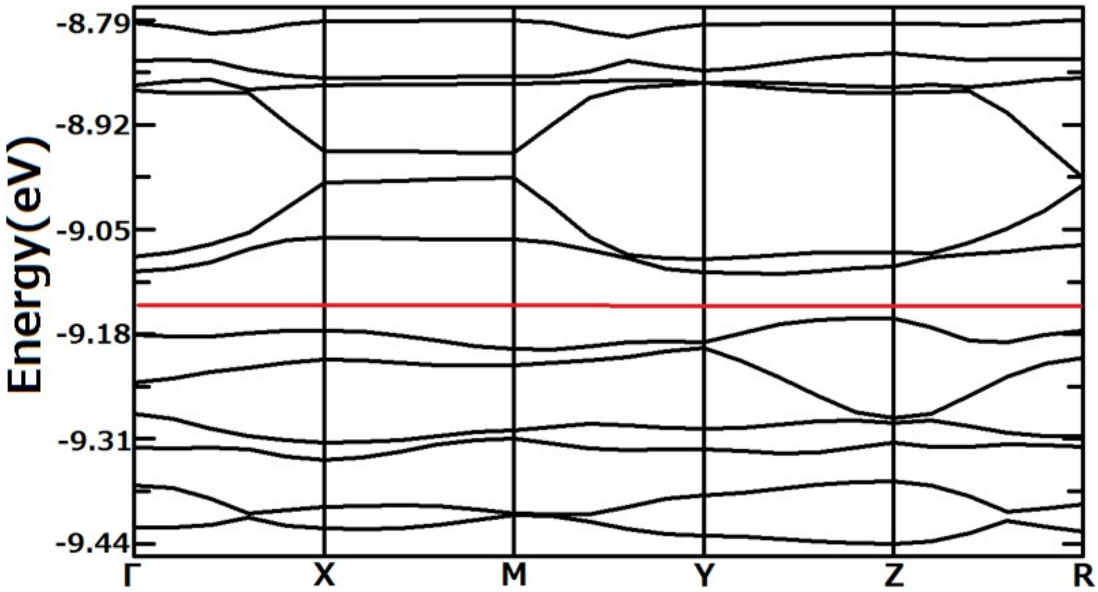

B

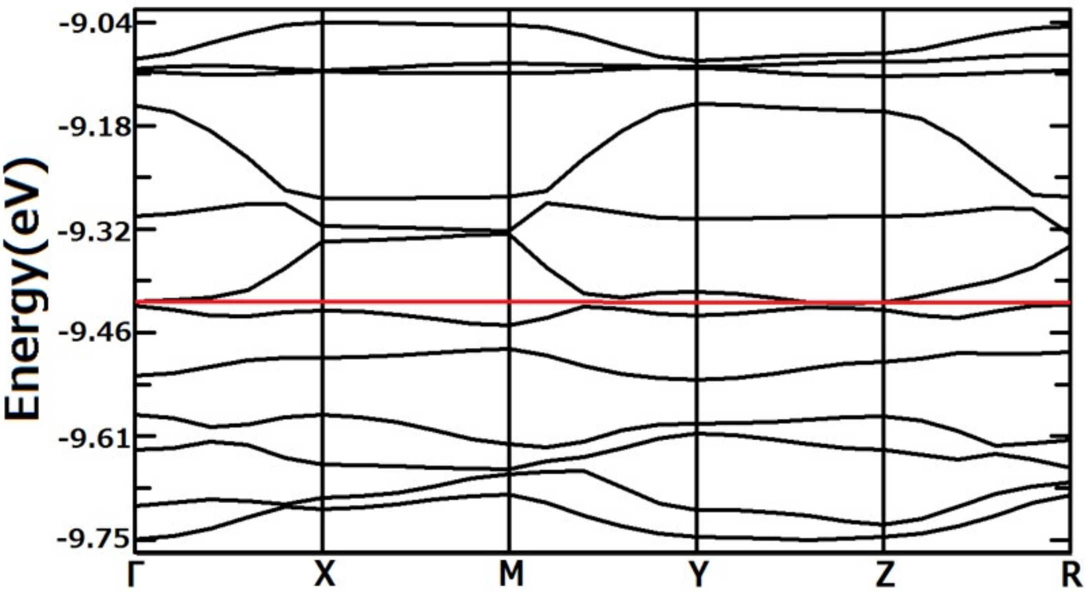

Figure S5.

Calculated tight-binding band structure for BPY[Ni(dmit)$_2$]$_6$·3CH$_3$CN using the parameters shown in (**A**) **Table S2A** (basis set "CRMM") and those shown in (**B**) **Table S2B** (basis set "Collected").[S1] The red line indicates the calculated Fermi level (E_F = -9.14 eV (**A**) and - 9.42 eV (**B**)). Γ, X, M, Y, Z, and R indicate points in reciprocal space ((0,0,0), (0.5,0,0), (0.5,0.5,0), (0,0.5,0), (0,0,0.5), and (0.5,0.5,0.5), respectively). As the crystal structure is in borderline cases between insulators and metals, small differences in parameters lead to qualitatively different band structures, i.e., (A) insulating and (B) metallic band structures. The observed physical properties are well explained based on **Figure S5A**.

C

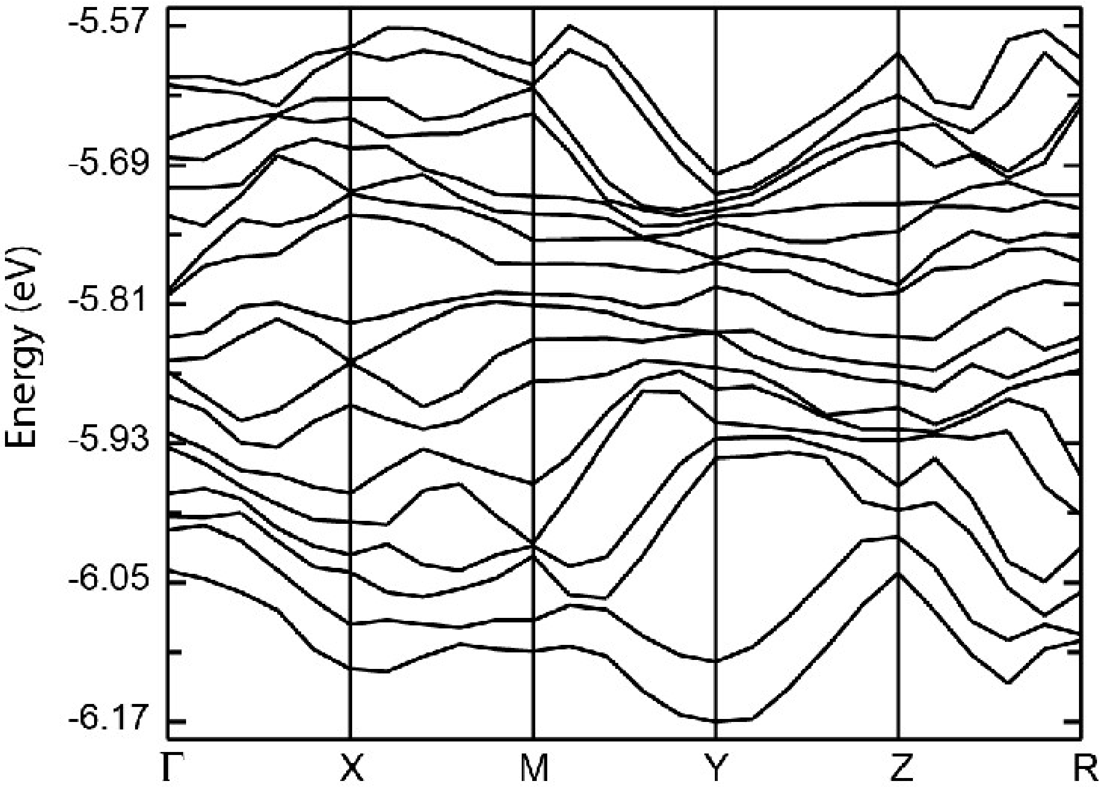

Figure S5 (Continued).
(**C**) Calculated tight-binding band structure for BPY[Ni(dmit)$_2$]$_6$·3CH$_3$CN using the parameters shown in (**A**) **Table S2A** (basis set “CRMM”).[S1] UV irradiation by 375 nm corresponds to the optical excitation of the electrons at E_F to the bands located around -5.87 eV. All these bands in **Figure S5C** are comprised of Ni(dmit)$_2$ molecular orbitals. Γ, X, M, Y, Z, and R indicate points in reciprocal space ((0,0,0), (0.5,0,0), (0.5,0.5,0), (0,0.5,0), (0,0,0.5), and (0.5,0.5,0.5), respectively).

Table S2.

A H_{ii} and ζ used in the band calculation[a)] (basis set "CRMM")

atom	atomic orbital	H_{ii} (eV)	ζ_1	c_1	ζ_2	c_2
Ni	4s	-7.25	2.077	0.4929	1.139	0.6188
	4p	-4.29	1.470	1.0000	0	0
	3d	-18.0	6.706	0.4212	2.874	0.7066
S	3s	-23.9	2.662	0.5990	1.688	0.5246
	3p	-11.9	2.338	0.5377	1.333	0.5615
C	2s	-19.2	1.831	0.7931	1.153	0.2739
	2p	-11.8	2.730	0.2595	1.257	0.8026
N	2s	-25.7	2.261	0.7297	1.425	0.3455
	2p	-15.4	3.249	0.2881	1.499	0.7783
H	1s	-13.6	1.300	1.0000	0	0

B H_{ii} and ζ used in the band calculation[a)] (basis set "Collected")

atom	atomic orbital	H_{ii} (eV)	ζ_1	c_1	ζ_2	c_2
Ni	4s	-9.17	1.825	1.0000	0	0
	4p	-5.15	1.125	1.0000	0	0
	3d	-13.49	5.750	0.5683	2.000	0.6292
S	3s	-20.0	2.662	0.5564	1.688	0.4873
	3p	-13.3	2.338	0.5212	1.333	0.5443
C	2s	-21.4	1.831	0.7616	1.153	0.2630
	2p	-11.4	2.730	0.2595	1.257	0.8025
N	2s	-26.0	1.950	1.0000	0	0
	2p	-13.4	1.950	1.0000	0	0
H	1s	-13.6	1.300	1.0000	0	0

[a)] H_{ii} = -VSIP (valence-state ionization potential [eV]). The single-zeta (for Ni 4p and H 1s) or double-zeta (for the remaining orbitals) Slater type orbitals (STOs) are used;

$$\chi_\mu(r,\theta,\phi) \propto r^{n-1}\exp(-\zeta r)Y(\theta,\phi) \text{ (single-zeta STO)}$$

$$\chi_\mu(r,\theta,\phi) \propto r^{n-1}[c_1\exp(-\zeta_1 r)+c_2\exp(-\zeta_2 r)]Y(\theta,\phi) \text{ (double-zeta STO)}$$

Table S3.

Calculated overlap and transfer integrals and the shortest sulfur-sulfur distances between adjacent Ni(dmit)$_2$ anions in BPY[Ni(dmit)$_2$]$_6$·3CH$_3$CN.

Interacting pair [a)]	$S_{ij}\times10^3$ [b)]	H_{ij} (meV) [c)]	S-S distances (Å) [d)]
① (6-6)	-21.3	478.7	3.741(2)
② (6-1)	-24.7	551.5	3.738(2)
③ (1-2)	24.6	-550.0	3.712(2)
④ (2-3)	-0.80	13.3	3.641(2)
⑤ (3-4)	0.20	-36.5	3.634(2)
⑥ (4-5)	-25.0	588.1	3.679(2)
⑦ (5-5)	7.3	-158.7	3.674(2)
⑧ (5-2)	-1.6	39.0	3.626(2)
⑨ (2-1)	-1.0	25.6	3.493(2)
⑩ (4-3)	1.1	-27.7	3.546(1)
⑪ (3-6)	-1.4	35.0	3.540(1)
⑫ (3-4)	-1.6	39.0	3.546(1)
⑬ (4-6)	-1.5	36.9	3.540(1)
⑭ (2-5)	-1.6	39.0	3.626(2)
⑮ (5-1)	-1.1	28.8	3.535(1)

[a)] See **Figure S6**. The numbers in parentheses indicate the interacting molecular pair. Other interactions are negligible. [b)] Overlap integrals calculated with a tight-binding approximation and the parameters in **Table S2A**. [c)] Transfer integrals calculated with a tight-binding approximation and the parameters in **Table S2A**. [d)] Intermolecular distances defined by the shortest sulfur-sulfur distances between the indicated pair of Ni(dmit)$_2$ anions. Note that all the intercolumnar interactions (⑧–⑮) are nearly equal.

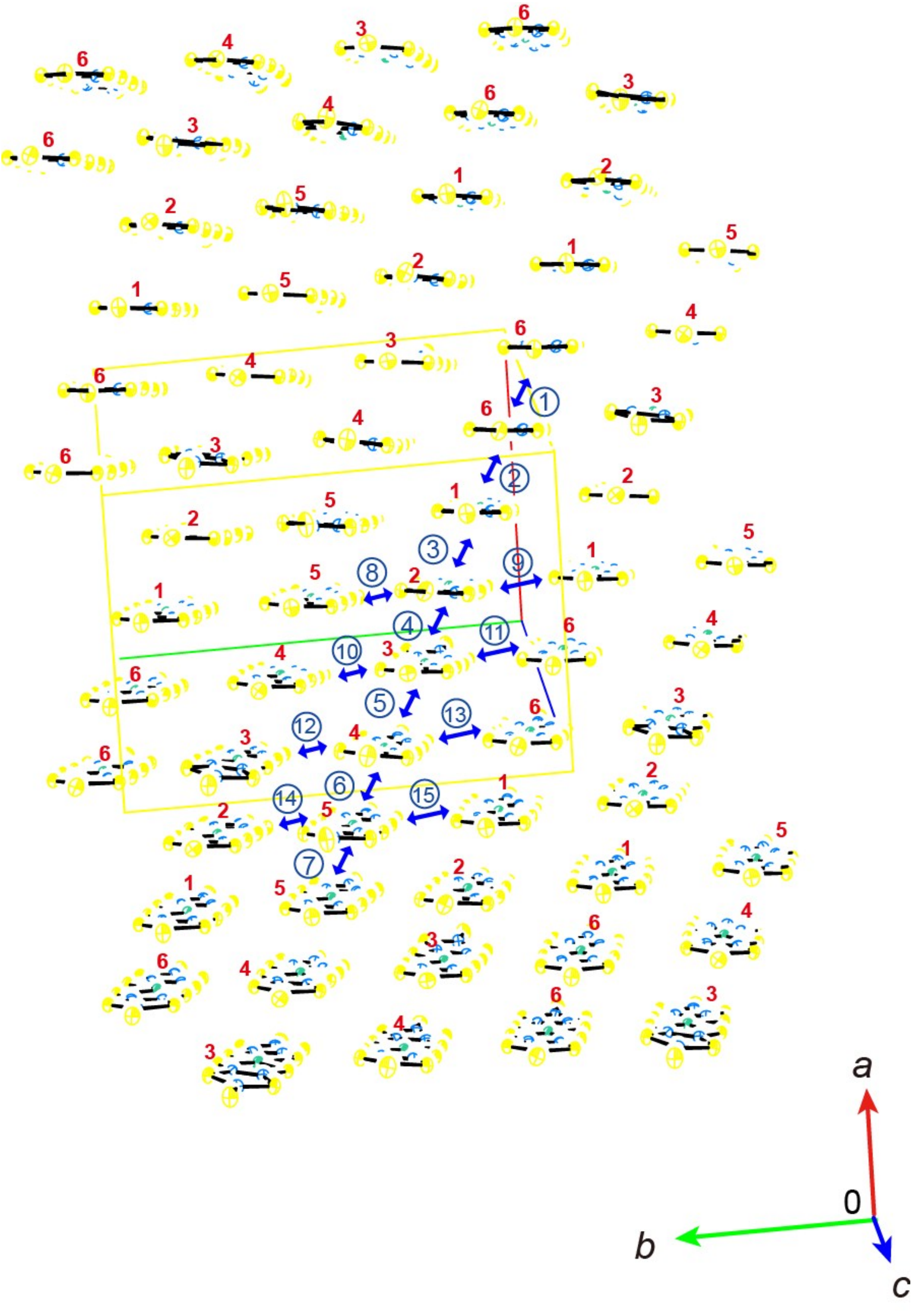

Figure S6

Interacting pairs of Ni(dmit)$_2$ anions in BPY[Ni(dmit)$_2$]$_6$·3CH$_3$CN. The numbers ①–⑮ correspond to those in **Table S3**. The numbers 1–6 in red correspond to those in **Figures 1** and **S3**, indicating the crystallographically independent Ni(dmit)$_2$ molecules.

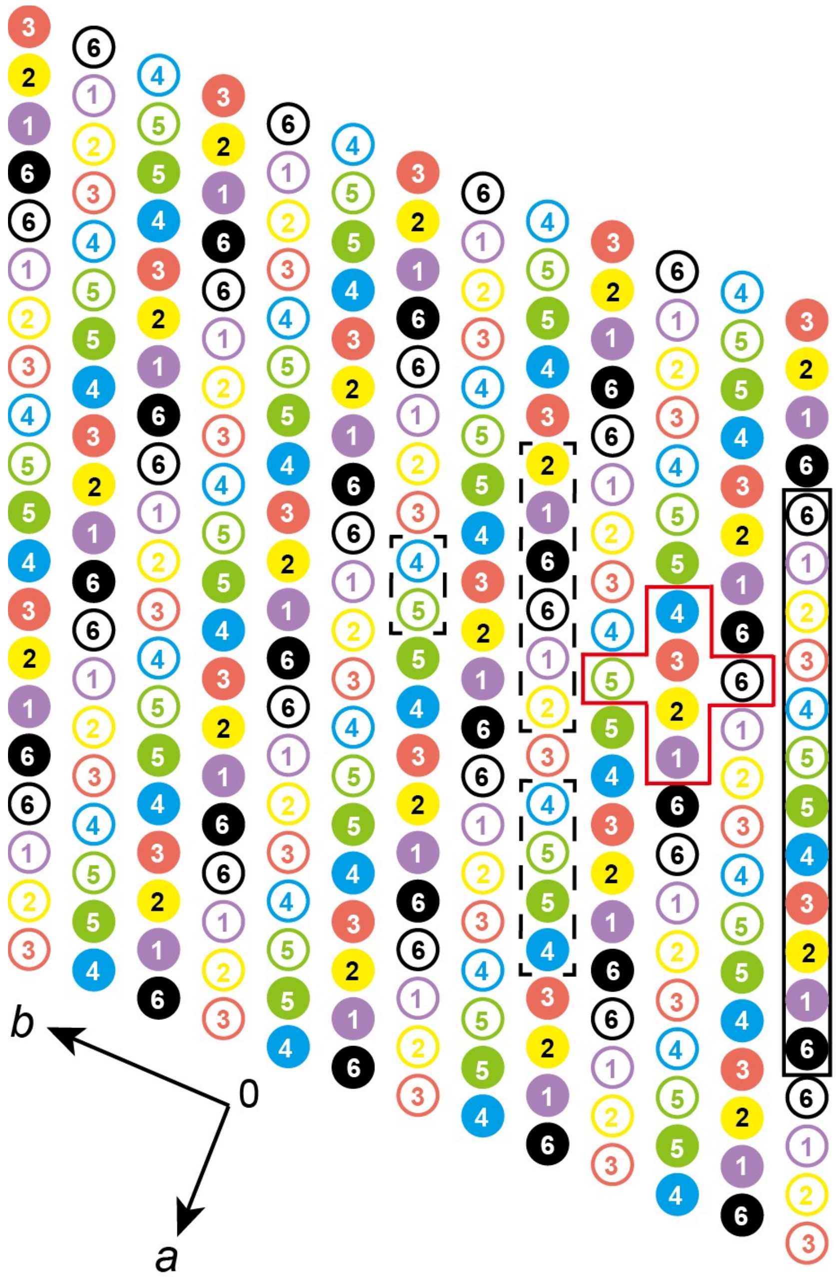

Figure S7

Schematic representation of the possible patterns of the intermolecular grouping to form e.g., a dimer, a tetramer, and a hexamer in BPY[Ni(dmit)$_2$]$_6$·3CH$_3$CN. The six crystallographically independent Ni(dmit)$_2$ anions are indicated by different colored circles, and the numbers correspond to those in **Figures 1** and **S3**. Open and filled circles of the same color are related to each other by an inversion center. The asymmetric unit shown in **Figure 1B** is highlighted by the red lines in this figure. The black solid rectangle shows the twelve-fold period of the superstructure along the stack. Lattice deformation involving the molecular grouping indicated by broken rectangles should pair the unpaired electrons.

§4. Spectroscopy

Raman spectra were measured for the single crystals using a microscope spectrometer (Renishaw in Via, Reflex, YAG 532 nm, 150 mW, spot size 1.4 µm, resolution 1.54 cm^{-1}) at 23 °C. The attenuated (1%) incident light was shed on the *ac*- and *bc*-planes with polarization parallel with the long molecular axis of the Ni(dmit)$_2$ species (~ // *c*-axis). The measurement was repeated on different spots on the same crystal face in addition to different crystals for confirmation of reproducibility and checking sample dependence.

IR spectra (450–4000 cm^{-1}, KBr pellets) were measured at 293 K using an FT-720 FREEXACT-II Fourier transform infrared spectrometer (Horiba) at a resolution of 2 cm^{-1}.

The DFT calculations (unrestricted, B3LYP/6-31G) of IR and Raman spectra were carried out using Gaussian 09 and GaussView 5.0.[S3,S4] The atomic parameters obtained from the X-ray structural analysis were utilized in the calculation without carrying out structure optimization, and imaginary frequencies were ignored. Each of the six Ni(dmit)$_2$ species in the asymmetric unit was calculated independently. As partially charged species cannot be calculated, the calculation was carried out for both cases of $[Ni(dmit)_2]^-$ (mono-radical, doublet) and $[Ni(dmit)_2]^0$ (neutral, singlet).

Solution spectra in the UV-Vis (200-1100 nm) region were measured in CH_3CN using a V-630 spectrophotometer (JASCO) at 293 K with a resolution of 2 nm.

The electron spin resonance (ESR) spectra of the X-band (9.3 GHz) were measured for the single crystals at 120–300 K using a JEOL JES FA100 equipped with a continuous flow-type liquid N_2 cryostat with a digital temperature controller (JEOL).[S2,S5,S6] All the single crystals used in the ESR measurements were briefly checked using X-ray oscillation photographs to identify the crystal quality and the directions of the crystallographic axes. The temperature was controlled so that the temperature variation did not exceed ± 0.5 K during the field sweep. A single crystal of $BPY[Ni(dmit)_2]_6 \cdot 3CH_3CN$ was mounted on a Teflon piece settled with a minimal amount of Apiezon N grease, sealed in a 5-mm-diameter quartz sample tube in a low-pressure (~20 mmHg) helium atmosphere. In some measurements, a single crystal of 1,1-diphenyl-2-picrylhydrazyl ($g = 2.00366 \pm 0.00004$) was also mounted on the Teflon piece beside $BPY[Ni(dmit)_2]_6 \cdot 3CH_3CN$ as an internal standard of the *g*-values. In the measurements under UV-irradiation, the standard sample was mounted on the opposite face of the Teflon piece to avoid UV irradiation of the standard sample.[S6] The magnetic field was corrected using a gauss meter (JEOL NMR Field Meter ES-FC5) at the end of every measurement. The time constant, sweep time, and modulation were 0.01 s, 30 s, and 100 kHz, respectively. Both dark and UV-irradiated spectra were measured under identical amplitudes, modulations, and time constants. Irradiation of the samples was carried out with the sample sealed in gaseous He under a reduced pressure in the ESR tube. The distance between the laser head and the sample was maintained at 50 mm. After 10 min of irradiation, the ESR signal became stable and constant, and the measurement was commenced with continuous irradiation. To examine the wavelength dependence of the photoresponse in the ESR measurements (**Figures S11A-S11M**), various light sources were utilized.

For UV-vis irradiation, a Hg/Xe lamp (SAN-EI Electric, SUPERCURE-203S; 200 W, 220-1100 nm) equipped with an appropriate band pass filter and a multimode quartz fiber optic light guide (core diameter: 5 mm, length: 1000 mm) were employed. The actual power at a given wavelength was estimated from the spectrum of the light source [I (mW cm^{-2} nm^{-1}) *vs.* λ (nm)] provided by the supplier. In some experiments, UV irradiation was carried out using a xenon light source (Asahi Spectra Co., Ltd., LAX-Cute 100; 100 W, 200–1100 nm) equipped with appropriate band pass filters ($\Delta\lambda$ = 40-60 nm), notch filters (UVA, UVB, VIS for 300–400, 240–300, and 400–700 nm, respectively), and a multimode quartz fiber optic light guide (core diameter: 5 mm, length: 1000 mm), or a UV laser (375 ± 5 nm, max 20 mW, NEOARK CORPORATION) equipped with focus and power adjusters. Infrared (IR) irradiation was carried out using a high-power tungsten-halogen lamp (Spectral Products, model ASBN-W100F-L; 100 W, 300-2600 nm) with an optical fiber (single mode, core diameter: 800 μm, length: 1000 mm) through SMA connectors. Further specifications for these light sources are provided in our previous papers.[S7,S8]

The ESR simulation was carried out in an anisotropic manner to identify the origin of the spectral features,[S2,S5,S6] using the Anisotropic Simulation software AniSim/FA ver. 2.2.0 by JEOL. The obtained parameters from the simulation are tabulated in **Tables S4A–S4D**. The obtained anisotropic parameters (g_x, g_y, and g_z) do not have the meanings of the principal values (g_{xx}, g_{yy}, and g_{zz}) related to molecular geometry and symmetry.

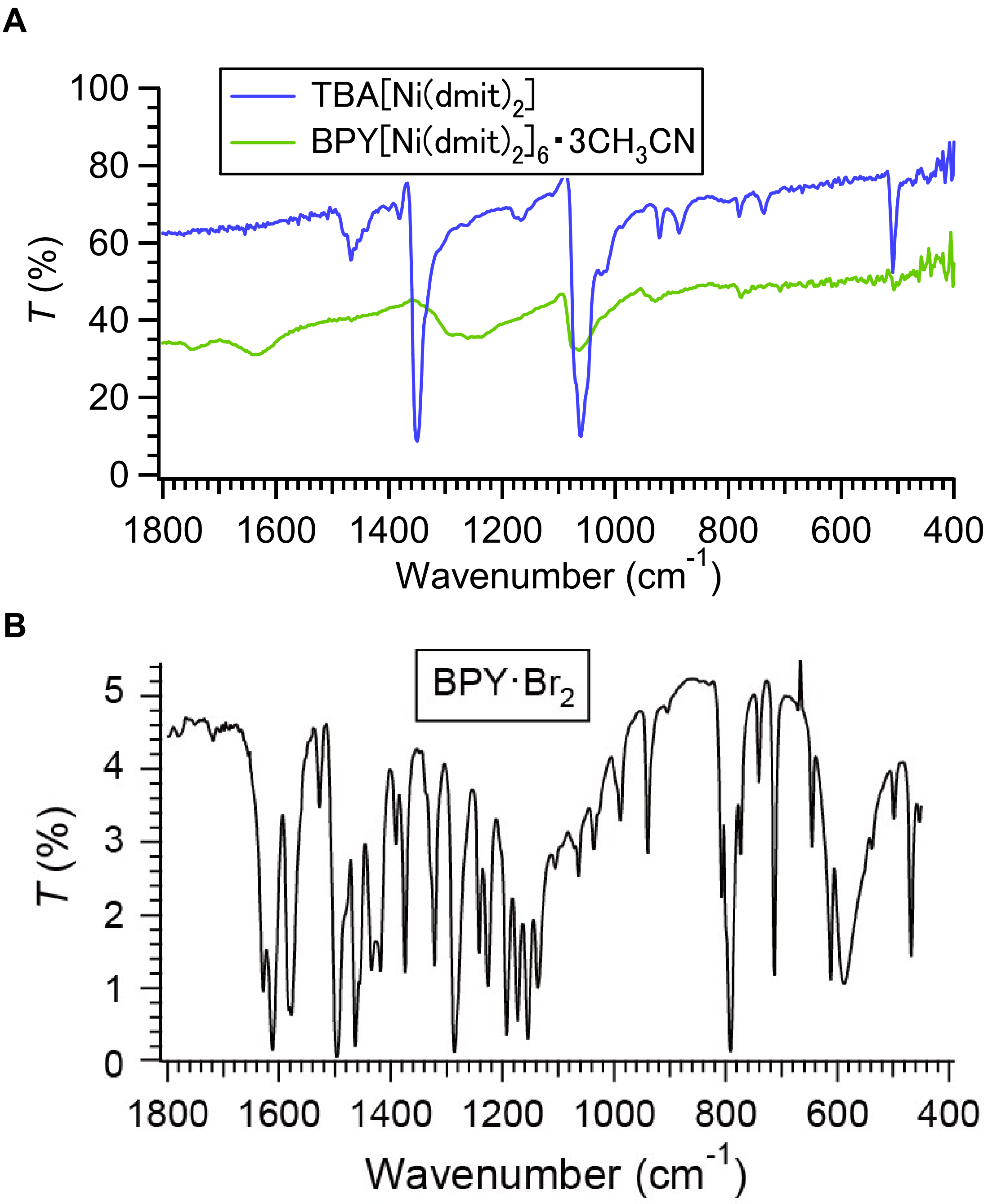

Figure S8.

IR spectra (fingerprint region) of (**A**) BPY$[Ni(dmit)_2]_6 \cdot 3CH_3CN$ and TBA$[Ni(dmit)_2]$ and (**B**) BPY$\cdot Br_2$ measured using KBr pellets. TBA designates the tetra(*n*-butyl)ammonium cation. In (**A**), broad peaks are observed at ~900–1100 cm^{-1} (C=S and C-S vibration modes), and ~1100-1400 cm^{-1} (C=C and C=S vibration modes), and ~750–800 cm^{-1} (C-S vibration modes) for BPY$[Ni(dmit)_2]_6 \cdot 3CH_3CN$. All the C=C peaks in the BPY$\cdot Br_2$ spectra are much sharper than those in the BPY$[Ni(dmit)_2]_6 \cdot 3CH_3CN$ spectra. This is consistent with the charge fluctuation on the $Ni(dmit)_2$ anions in BPY$[Ni(dmit)_2]_6 \cdot 3CH_3CN$. **Figure S8A** is cited from Ref. S2 with permission. Copyright 2012 American Chemical Society.

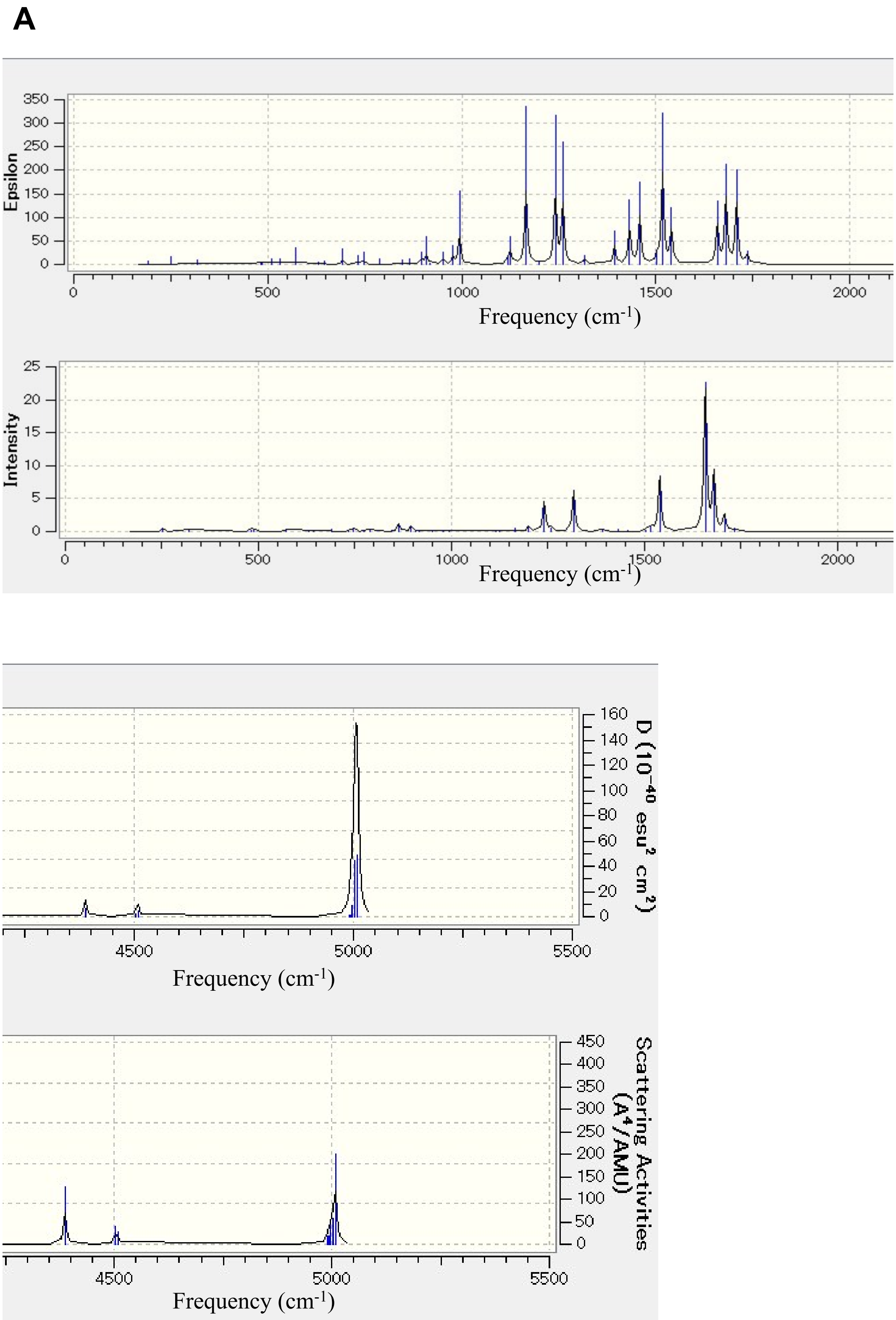

Figure S9.

(**A**) Calculated IR (upper) and Raman (lower) spectra using Gaussian 09 based on the observed molecular structure for BPY^{2+}.[S3,S4] For both spectra, there is no peak between ~2000 and ~4000 cm^{-1}. Note that the set of spectra are divided into two rows for clarity.

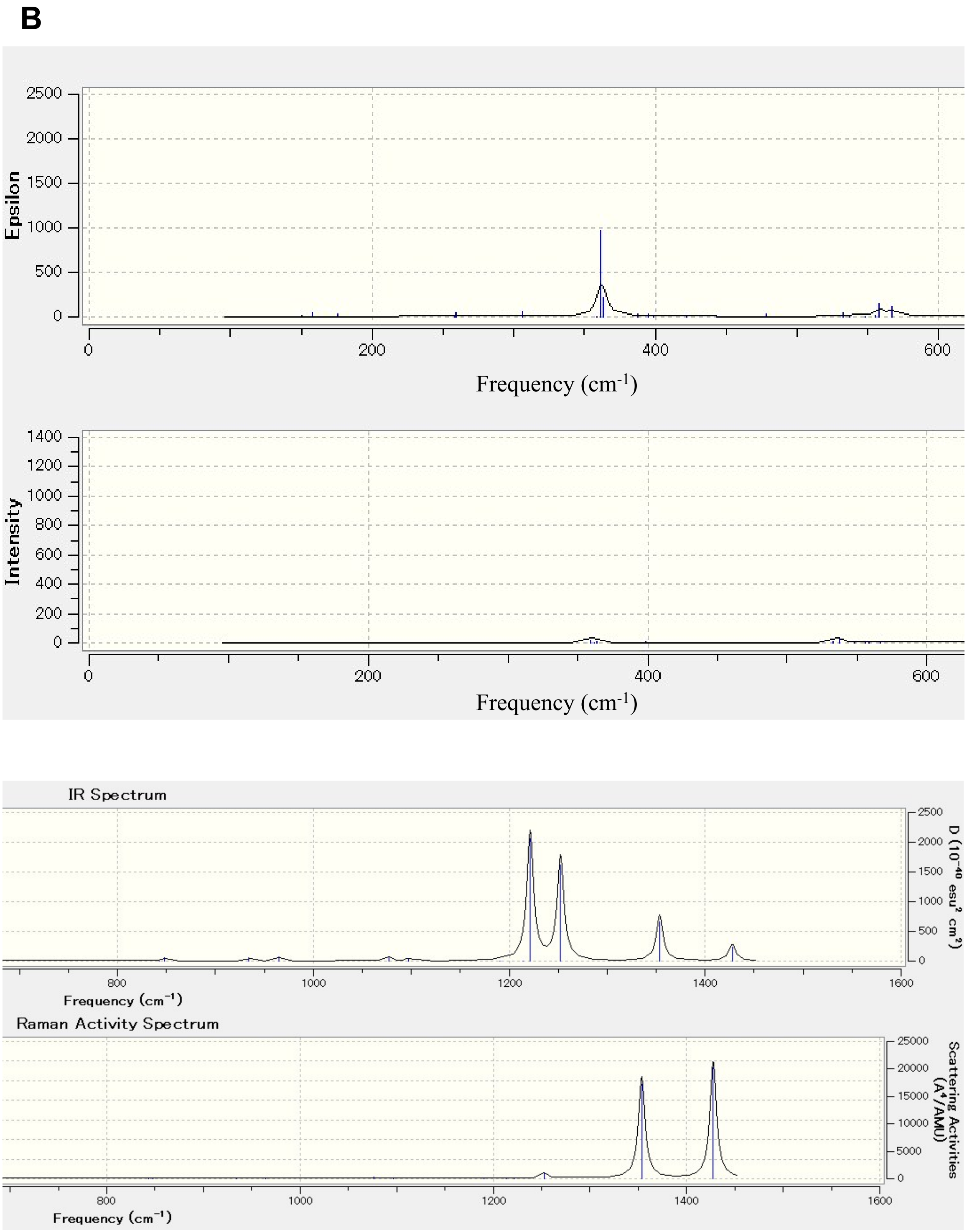

Figure S9 (continued).

(**B**) Calculated IR (upper) and Raman (lower) spectra using Gaussian 09 based on the observed molecular structure for $[Ni(dmit)_2]^{\delta -}$ containing Ni1 assuming $\delta = 1$.[S3,S4] For both spectra, there is no peak between ~600 and ~800 cm^{-1}. Note that the set of spectra are divided into two rows for clarity.

C

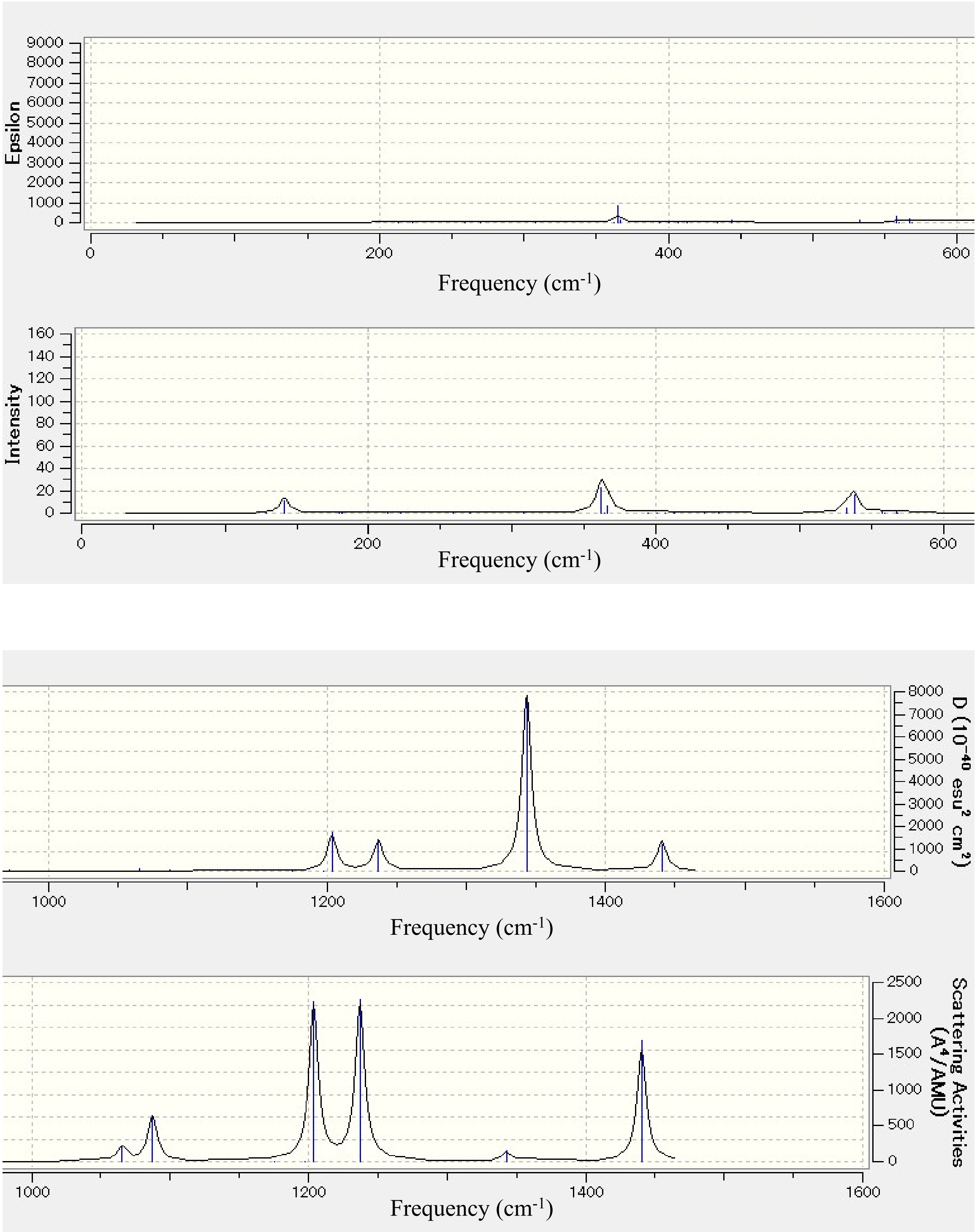

Figure S9 (continued).

(**C**) Calculated IR (upper) and Raman (lower) spectra using Gaussian 09 based on the observed molecular structure for [Ni(dmit)$_2$]$^{\delta-}$ containing Ni1 assuming $\delta = 0$.[S3,S4] For both spectra, there is no peak between ~600 and ~1000 cm^{-1}. Note that the set of spectra are divided into two rows for clarity.

D

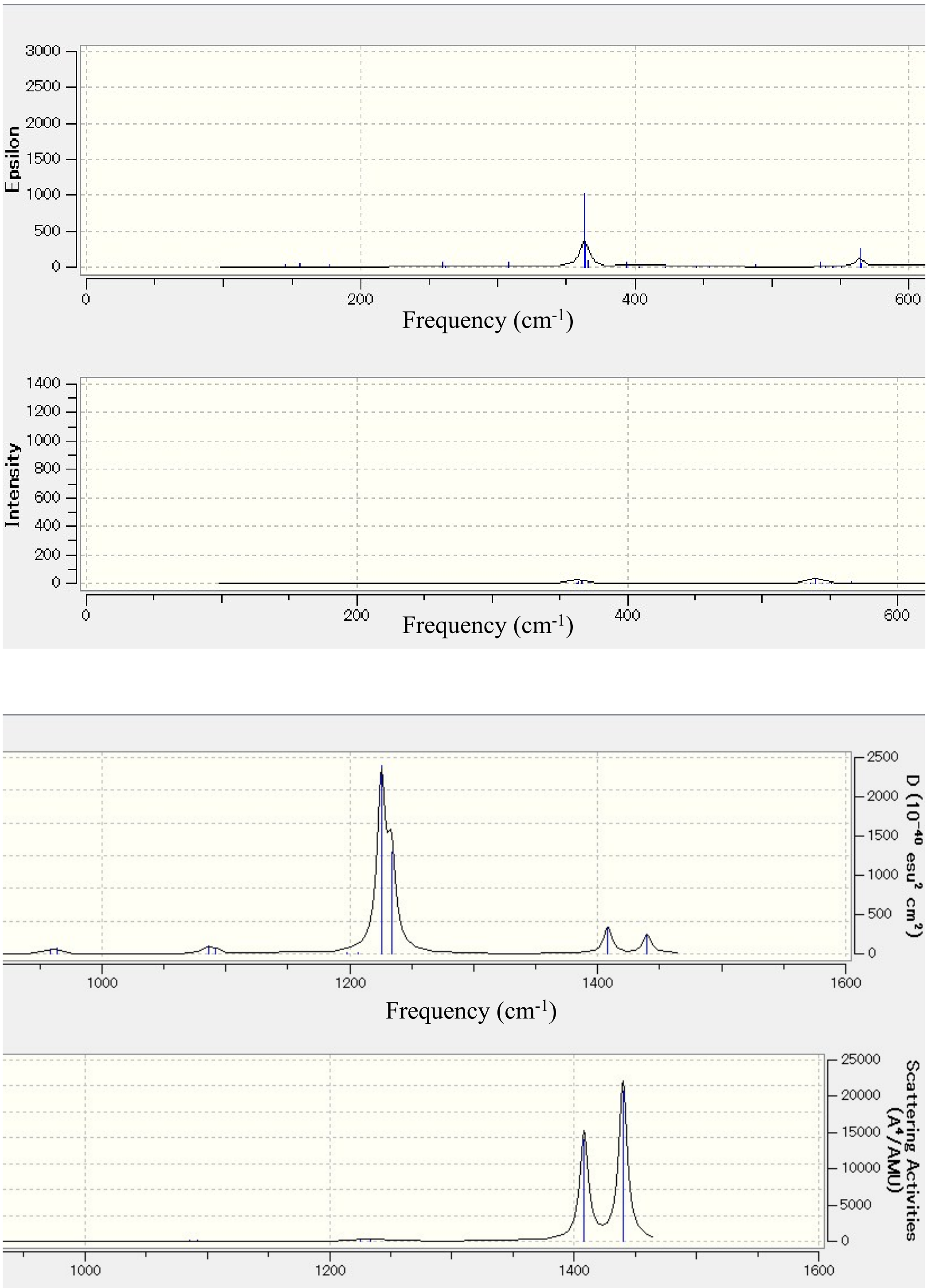

Figure S9 (continued).

(**D**) Calculated IR (upper) and Raman (lower) spectra using Gaussian 09 based on the observed molecular structure for $[Ni(dmit)_2]^{\delta-}$ containing Ni2 assuming $\delta = 1$.[S3,S4] For both spectra, there is no peak between ~600 and ~900 cm^{-1}. Note that the set of spectra are divided into two rows for clarity.

E

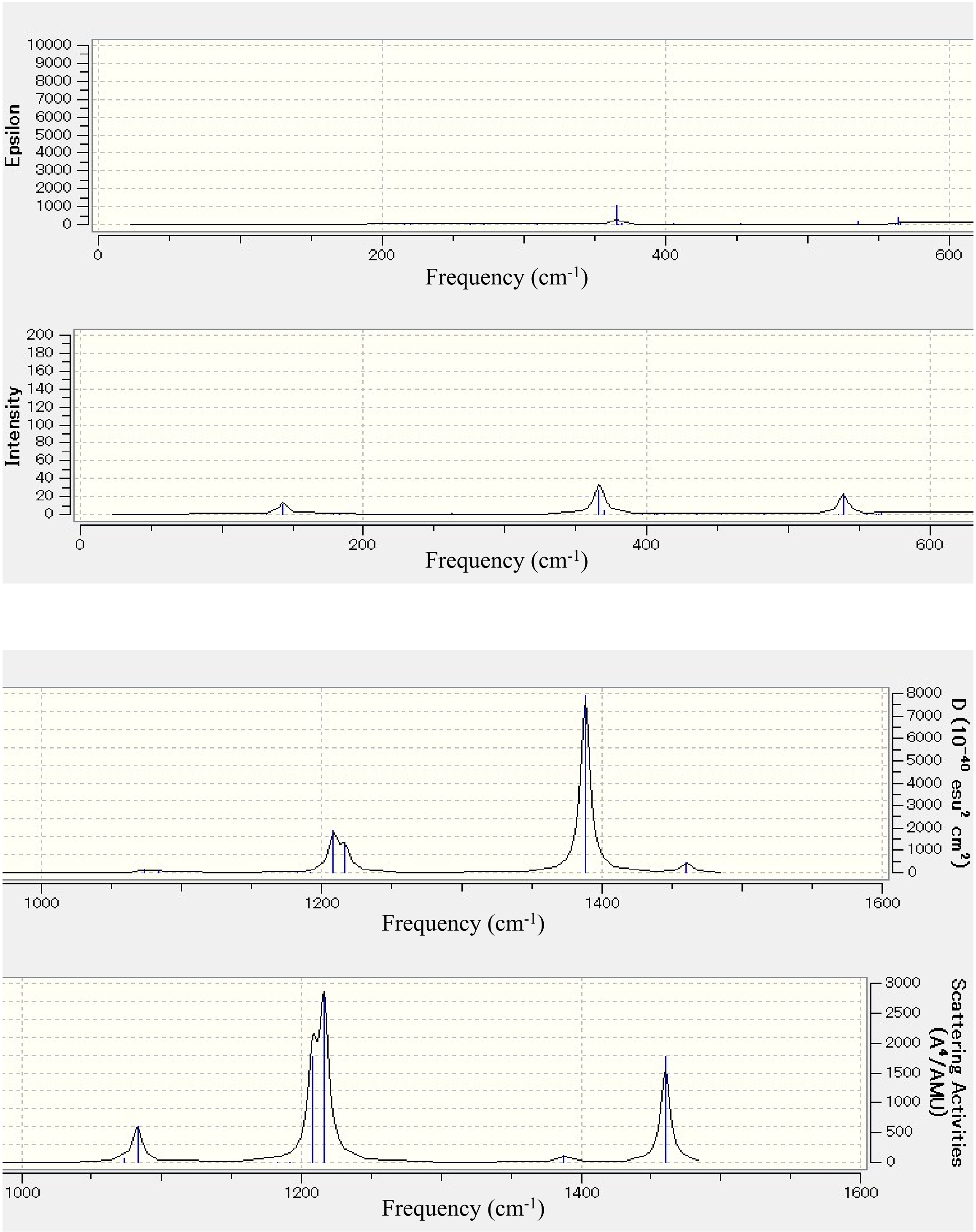

Figure S9 (continued).

(**E**) Calculated IR (upper) and Raman (lower) spectra using Gaussian 09 based on the observed molecular structure for [Ni(dmit)$_2$]$^{\delta-}$ containing Ni2 assuming $\delta = 0$.[S3,S4] For both spectra, there is no peak between ~600 and ~1000 cm^{-1}. Note that the set of spectra are divided into two rows for clarity.

F

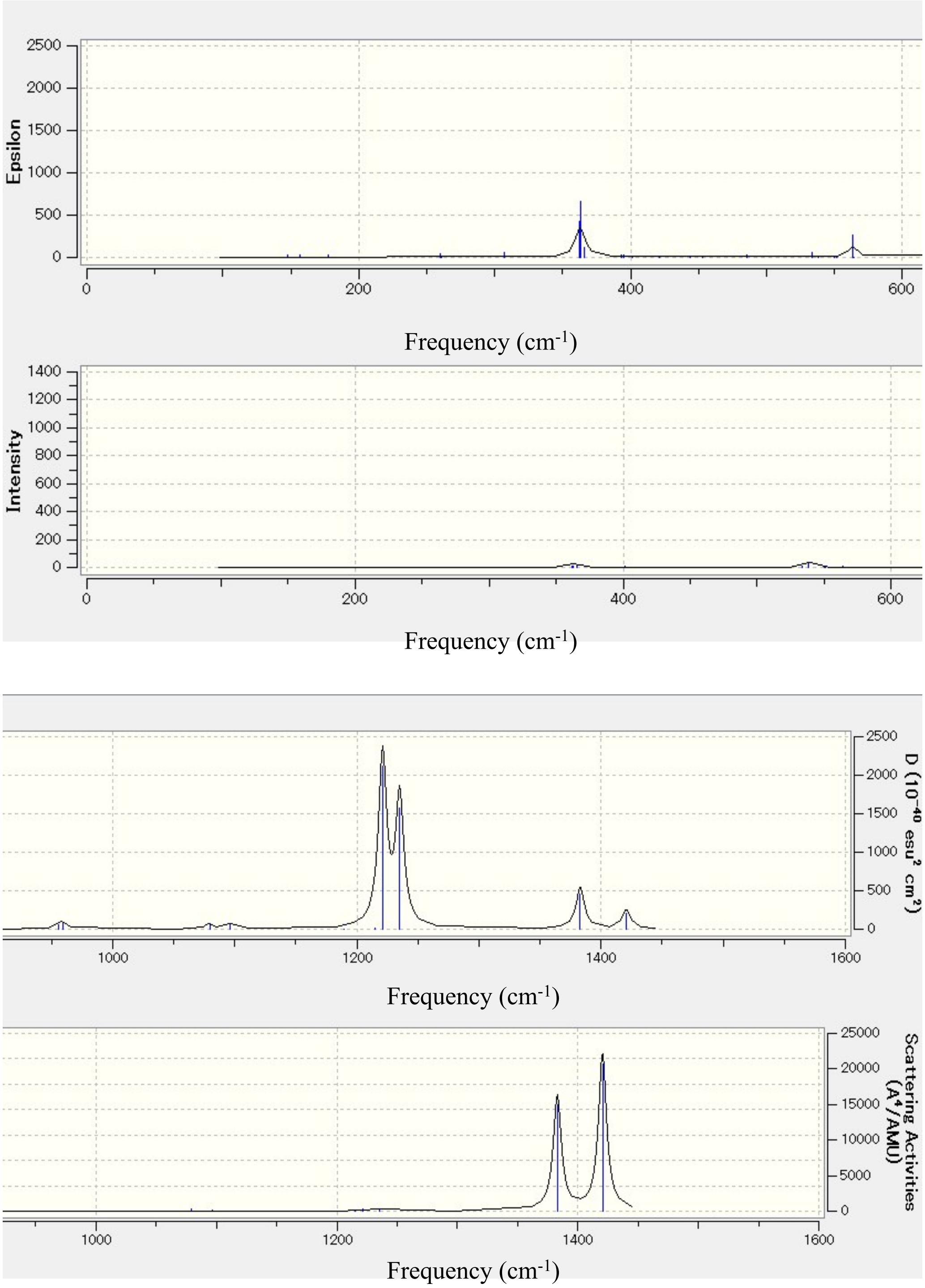

Figure S9 (continued).

(**F**) Calculated IR (upper) and Raman (lower) spectra using Gaussian 09 based on the observed molecular structure for $[\mathrm{Ni(dmit)_2}]^{\delta-}$ containing Ni3 assuming $\delta = 1$.[S3,S4] For both spectra, there is no peak between ~600 and ~900 cm^{-1}. Note that the set of spectra are divided into two rows for clarity.

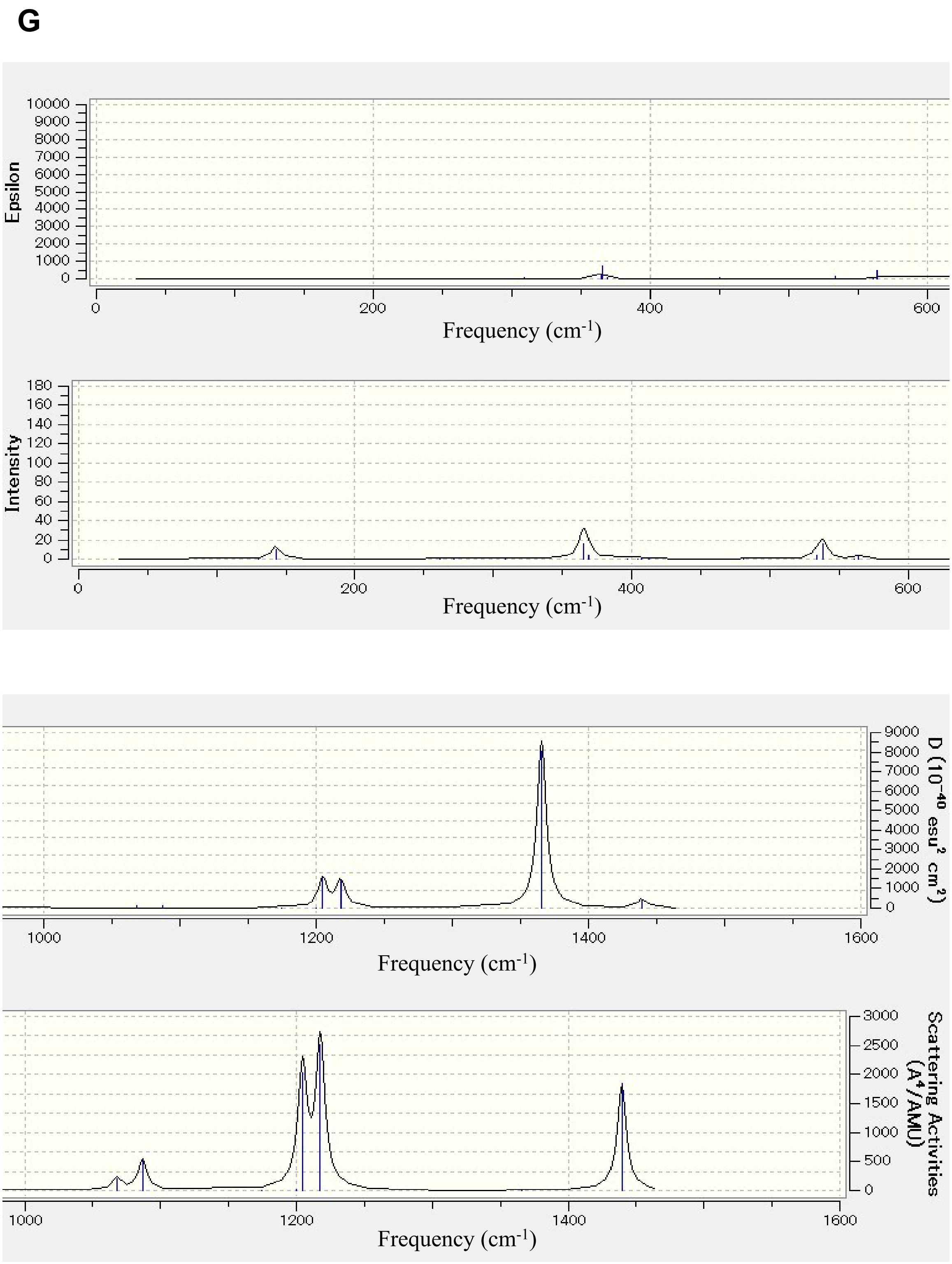

Figure S9 (continued).

(**G**) Calculated IR (upper) and Raman (lower) spectra using Gaussian 09 based on the observed molecular structure for $[Ni(dmit)_2]^{\delta-}$ containing Ni3 assuming $\delta = 0$.[S3,S4] For both spectra, there is no peak between ~600 and ~1000 cm^{-1}. Note that the set of spectra are divided into two rows for clarity.

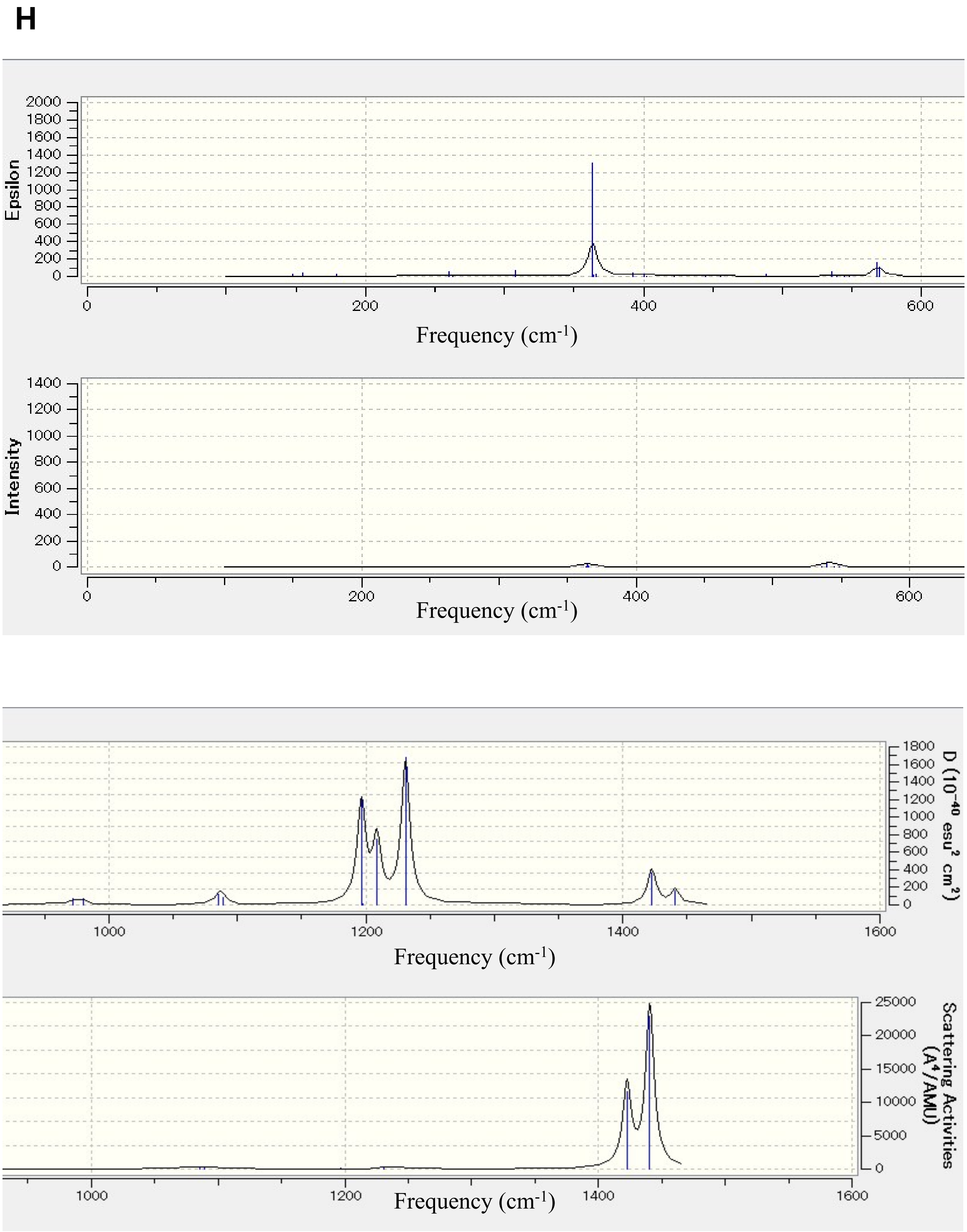

Figure S9 (continued).

(**H**) Calculated IR (upper) and Raman (lower) spectra using Gaussian 09 based on the observed molecular structure for $[Ni(dmit)_2]^{\delta-}$ containing Ni4 assuming $\delta = 1$.[S3,S4] For both spectra, there is no peak between ~600 and ~950 cm^{-1}. Note that the set of spectra are divided into two rows for clarity.

I

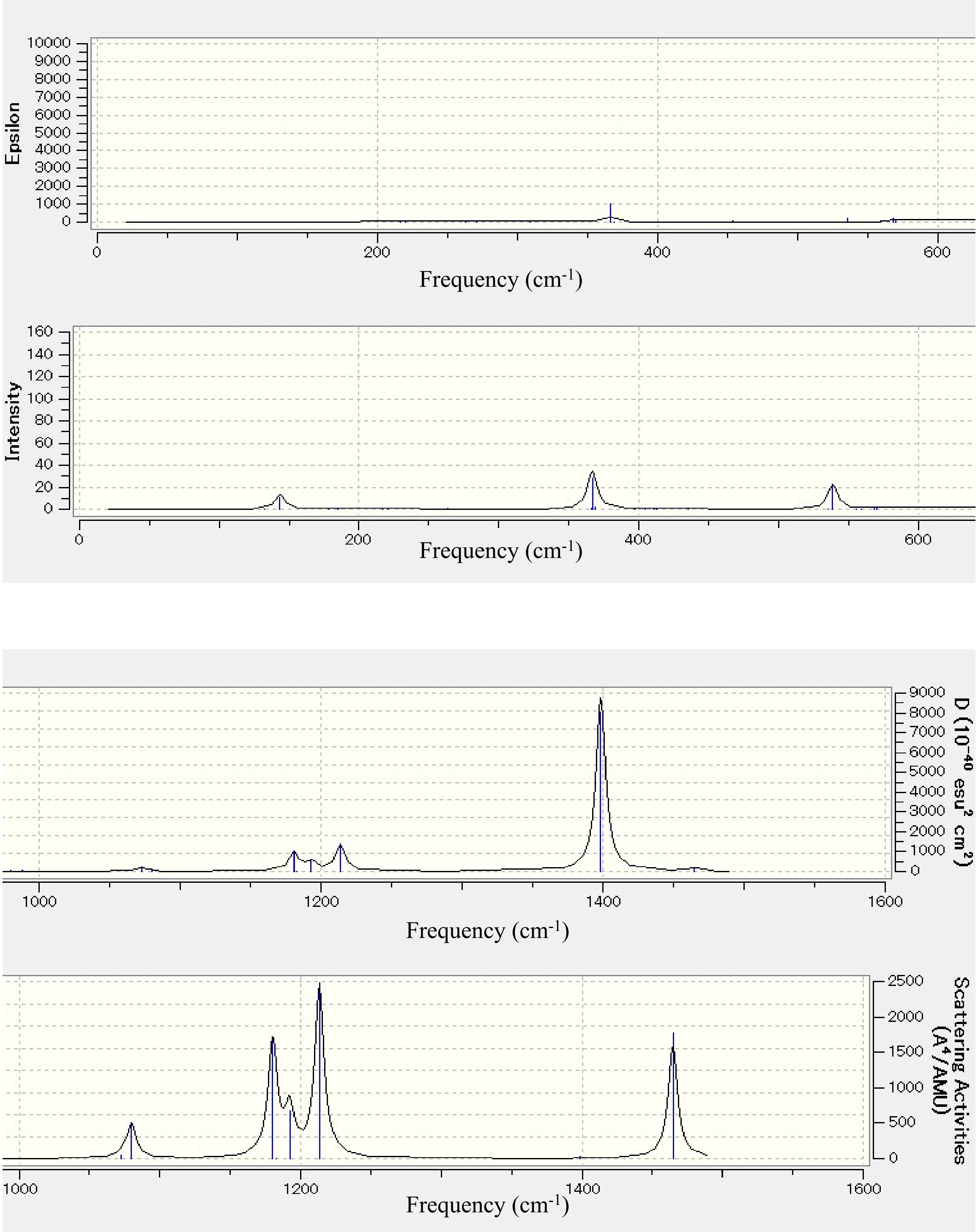

Figure S9 (continued).

(**I**) Calculated IR (upper) and Raman (lower) spectra using Gaussian 09 based on the observed molecular structure for $[Ni(dmit)_2]^{\delta-}$ containing Ni4 assuming $\delta = 0$.[S3,S4] For both spectra, there is no peak between ~600 and ~1000 cm^{-1}. Note that the set of spectra are divided in two rows for clarity.

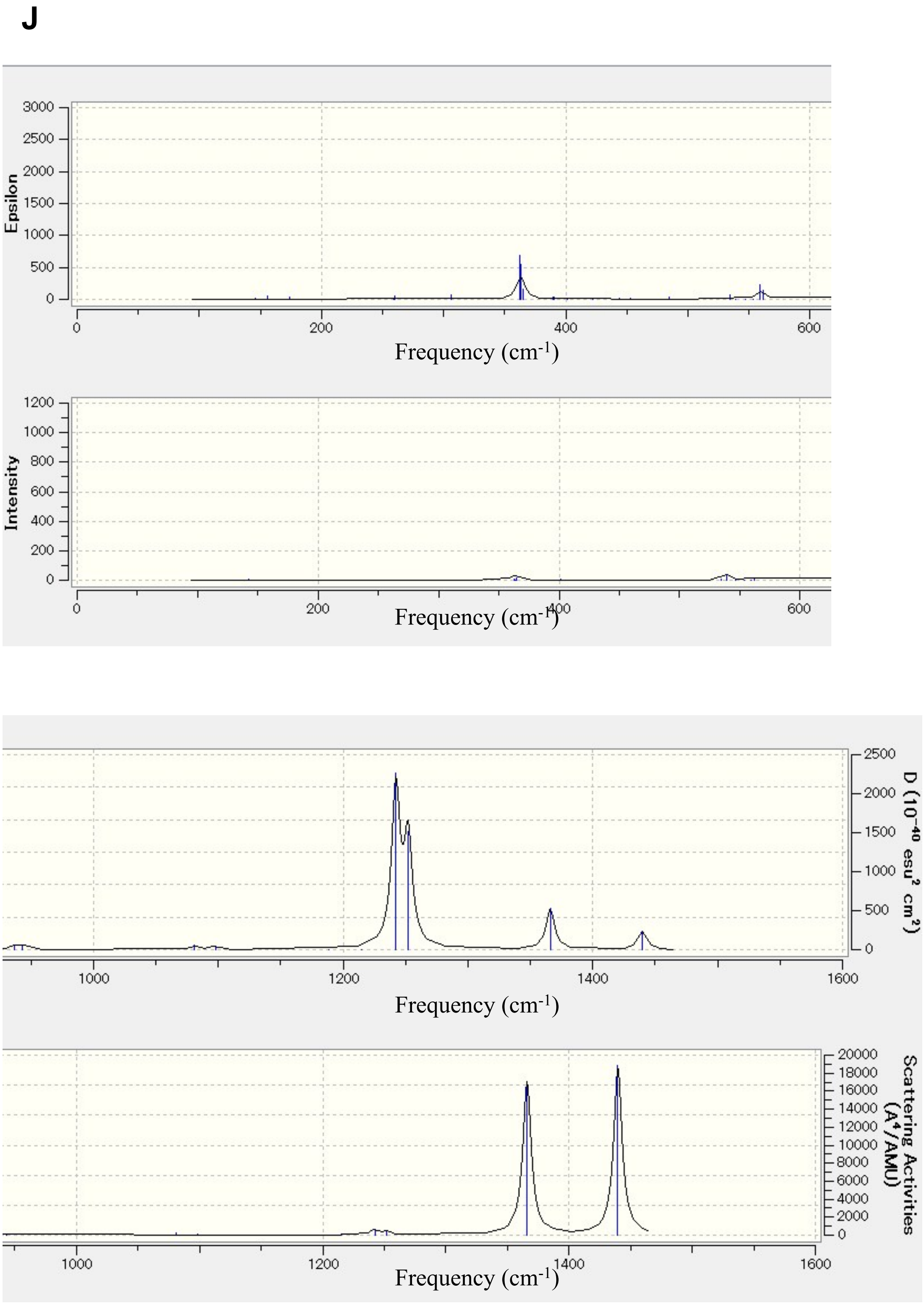

Figure S9 (continued).

(**J**) Calculated IR (upper) and Raman (lower) spectra using Gaussian 09 based on the observed molecular structure for $[\mathrm{Ni(dmit)_2}]^{\delta-}$ containing Ni5 assuming $\delta = 1$.[S3,S4] For both spectra, there is no peak between ~600 and ~900 cm^{-1}. Note that the set of spectra are divided in two rows for clarity.

K

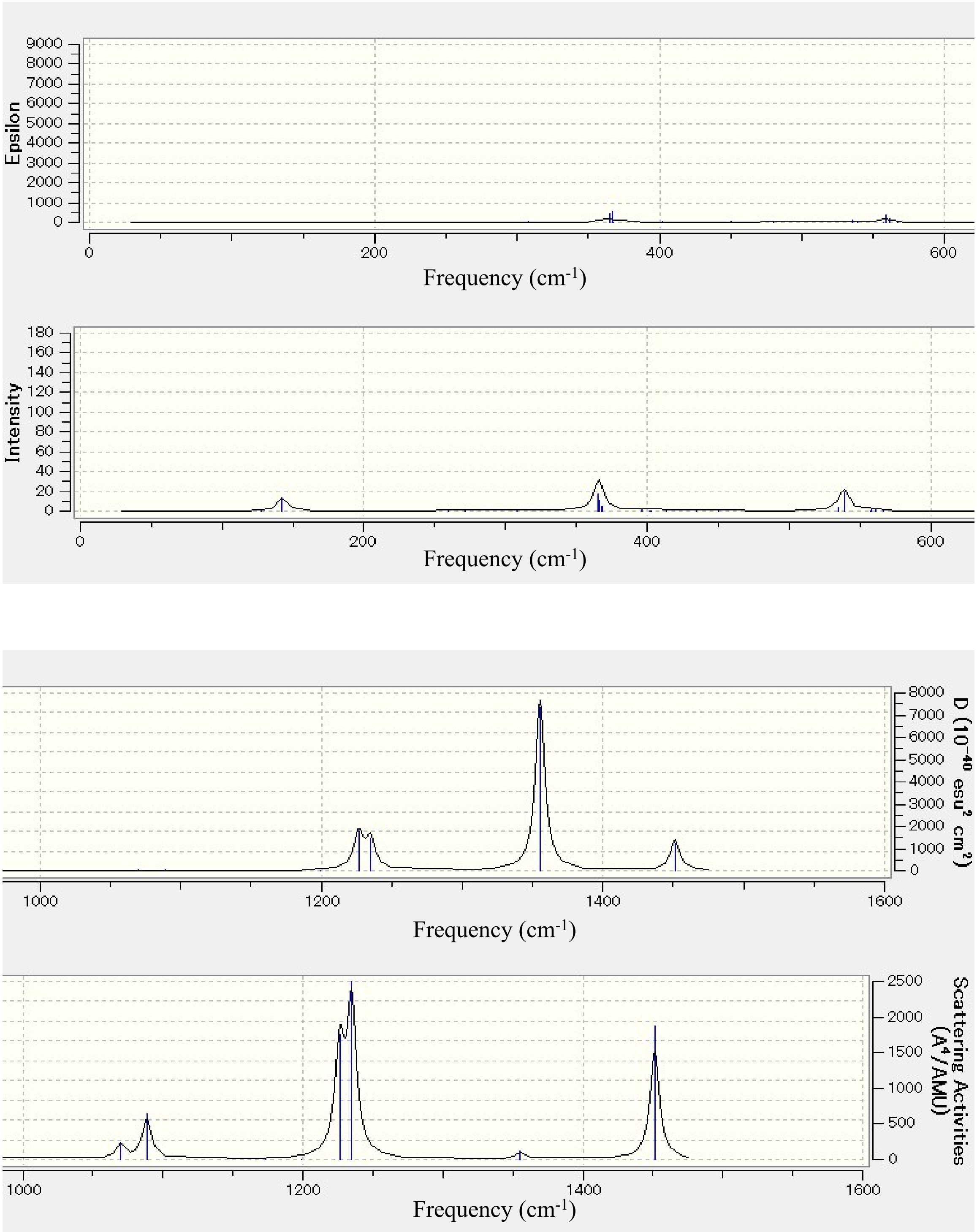

Figure S9 (continued).

(**K**) Calculated IR (upper) and Raman (lower) spectra using Gaussian 09 based on the observed molecular structure for $[Ni(dmit)_2]^{\delta-}$ containing Ni5 assuming $\delta = 0$.[S3,S4] For both spectra, there is no peak between ~600 and ~1000 cm^{-1}. Note that the set of spectra are divided into two rows for clarity.

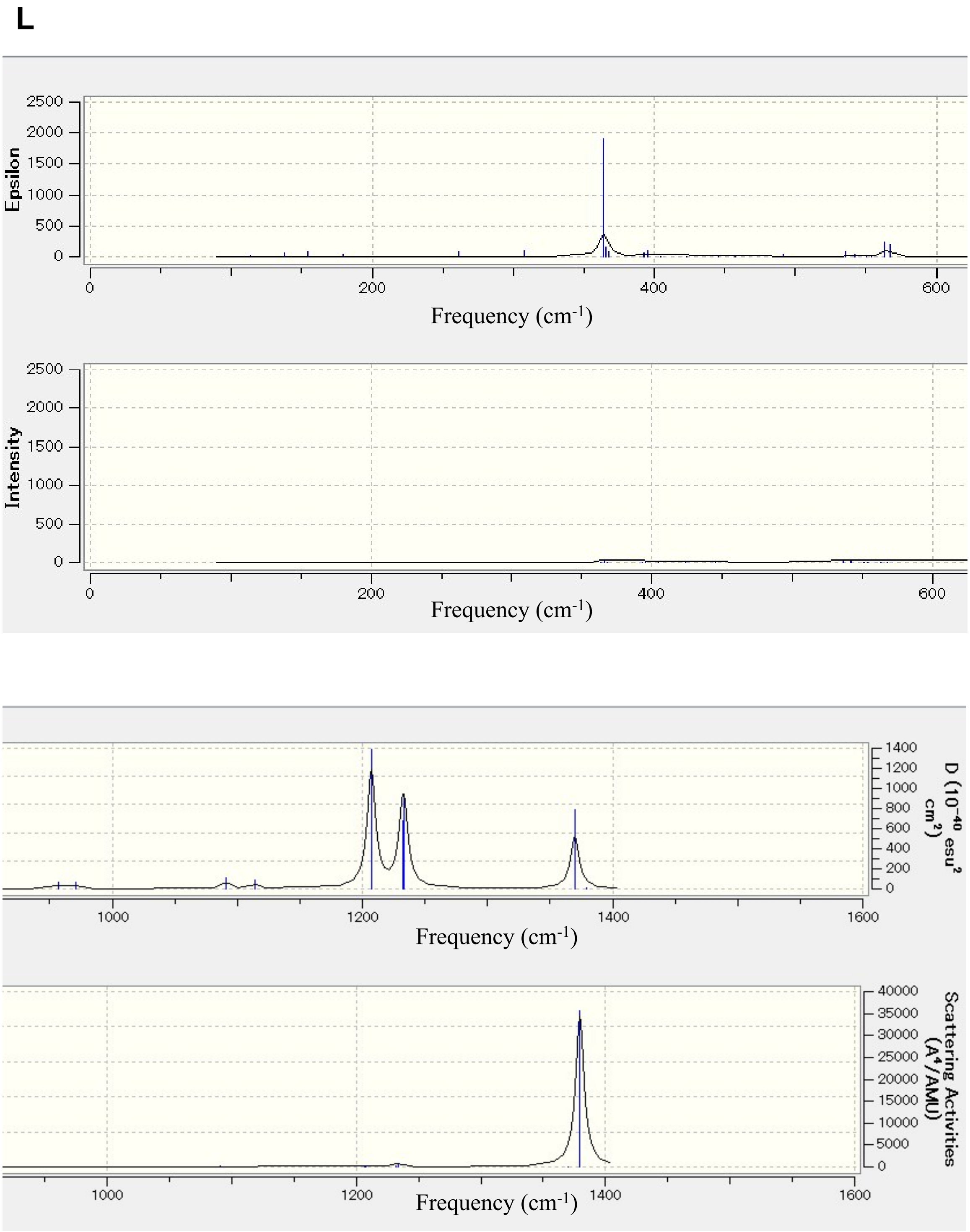

Figure S9 (continued).

(**L**) Calculated IR (upper) and Raman (lower) spectra using Gaussian 09 based on the observed molecular structure for $[Ni(dmit)_2]^{\delta-}$ containing Ni6 assuming δ = 1.[S3,S4] For both spectra, there is no peak between ~600 and ~950 cm^{-1}. Note that the set of spectra are divided into two rows for clarity.

M

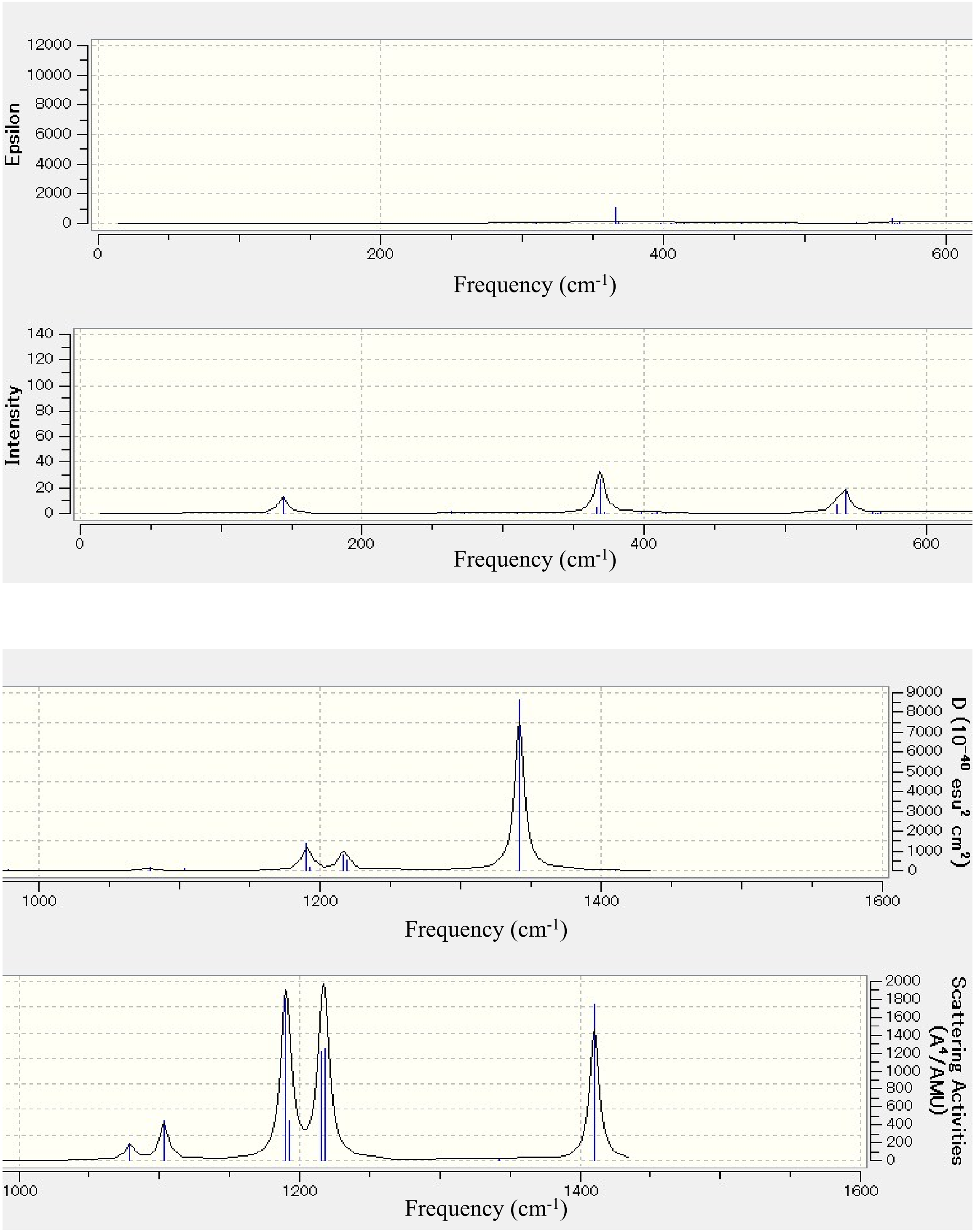

Figure S9 (continued).

(**M**) Calculated IR (upper) and Raman (lower) spectra using Gaussian 09 based on the observed molecular structure for $[Ni(dmit)_2]^{\delta-}$ containing Ni6 assuming $\delta = 0$.[S3,S4] For both spectra, there is no peak between ~600 and ~1000 cm^{-1}. Note that the set of spectra are divided into two rows for clarity.

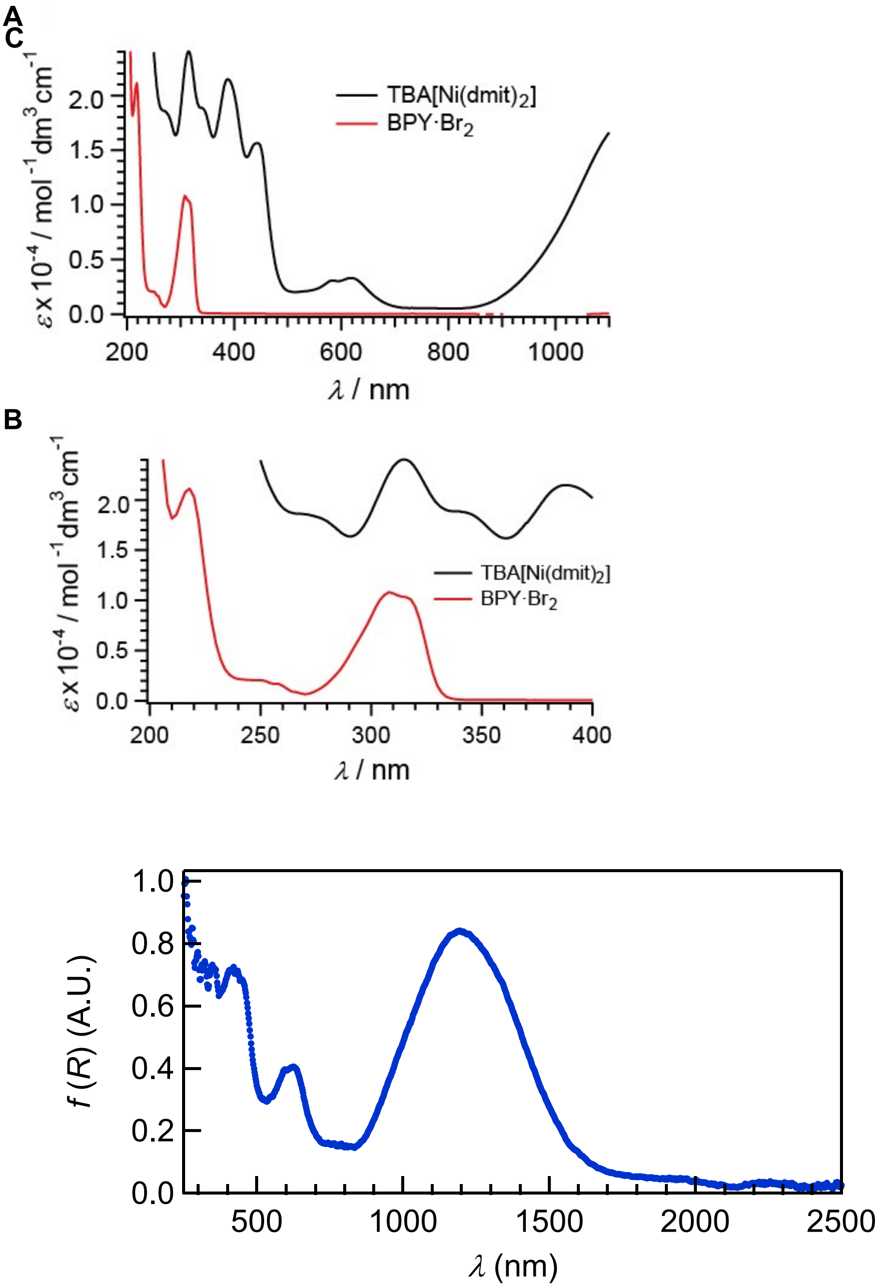

Figure S10.

UV-vis-NIR solution spectra in CH_3CN of TBA[Ni(dmit)$_2$] and BPY·Br_2 at 293 K. (**A**) Entire spectra and (**B**) expanded view of the UV region. (**C**) Diffuse reflectance spectrum of TBA[Ni(dmit)$_2$] (powder), where TBA designates the tetra(*n*-butyl)ammonium cation. These spectra prove that photoexcitation by the UV light of 375 nm selectively causes charge transfer between Ni(dmit)$_2$ anions in the 1:6 salt. (**A**) and (**B**) are adapted with permission from Ref. S2. Copyright 2012 American Chemical Society.

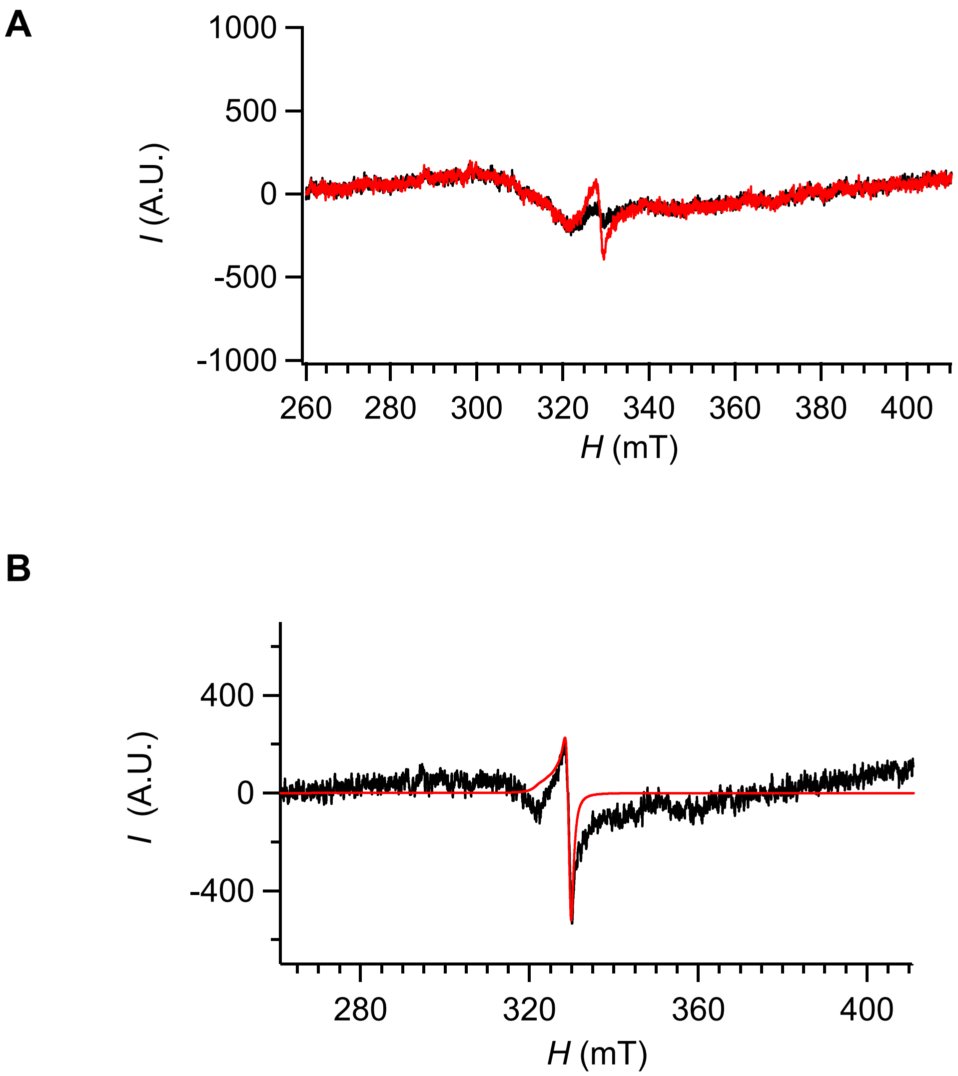

Figure S11.

(**A**) Electron spin resonance spectra for $\mathrm{BPY[Ni(dmit)_2]_6\cdot 3CH_3CN}$ (single crystal) under dark (**black**) and UV (375 ± 5 nm; 14.4 mW $\mathrm{cm^{-2}}$) irradiation (**red**) at 123 K. Magnetic field (*H*) // *b*-axis. The UV light was incident on the *ab*-plane.

(**B**) Electron spin resonance spectrum for $\mathrm{BPY[Ni(dmit)_2]_6\cdot 3CH_3CN}$ (single crystal) observed under UV (375 ± 5 nm; 14.4 mW $\mathrm{cm^{-2}}$) irradiation (**black**) at 123 K and simulated spectrum (**red**) using the parameters in **Table S4A**. The agreement of the two spectra demonstrates that the observed signal can be assigned to the spins on the BPY cations. The spectrum in black is a different one from that in red in **Figure S11A**. Magnetic field (*H*) // *b*-axis. The UV light was incident on the *ab*-plane.

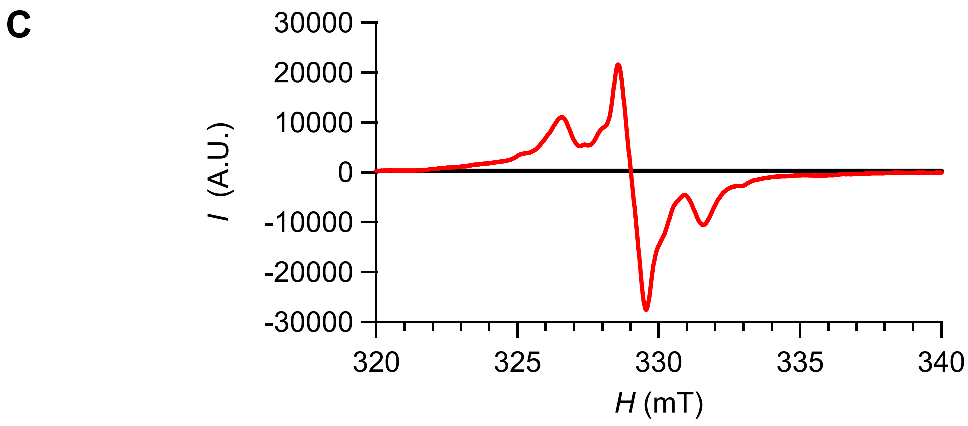

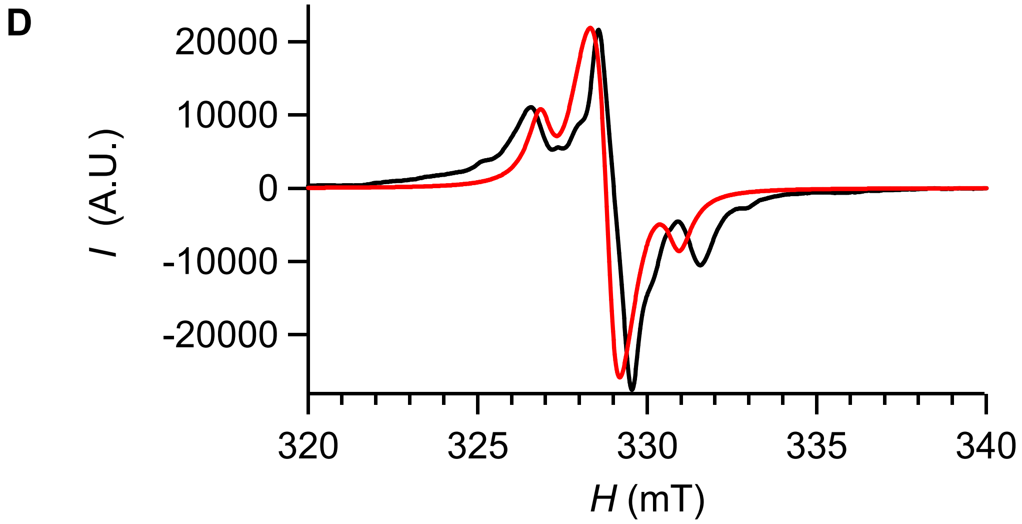

Figure S11 (Continued).

(**C**) Electron spin resonance spectra for BPY[Ni(dmit)$_2$]$_6$·3CH$_3$CN (single crystal) observed under dark (**black**) and a wider range of UV (250–450 nm; 6.7 W cm^{-2}) irradiation (**red**) at 123 K. Spectral simulation (**Figure S11D** and **Table S4B**) indicate that the observed signal under UV irradiation can be assigned to the spins on the BPY cations. The wider range of UV covers a larger portion of the absorption band of the BPY cations at ~270–330 nm (**Figure S10**). Therefore, the observed apparent enhancement in the ESR intensity under such UV irradiation is consistent with the absorption spectrum. Magnetic field (*H*) // *b*-axis. The UV light was incident on the *ab*-plane.

(**D**) Electron spin resonance spectrum for BPY[Ni(dmit)$_2$]$_6$·3CH$_3$CN (single crystal) observed under UV (250–450 nm; 6.7 W cm^{-2}) irradiation (**black**) at 123 K and simulated spectrum (**red**). The moderate agreement between the two spectra demonstrated that the observed signal can be assigned to the spins on the BPY cations. The spectrum in **black** is the same one as that in **red** in **Figure S11C**. Magnetic field (*H*) // *b*-axis. The UV light was incident on the *ab*-plane.

E

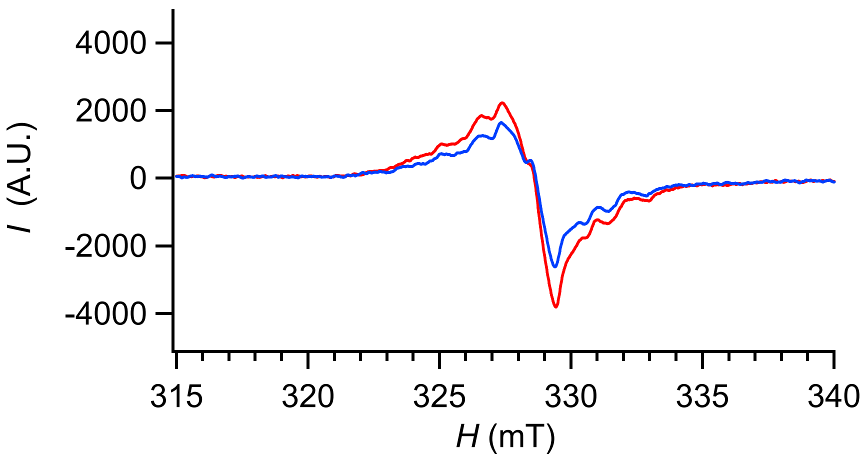

F

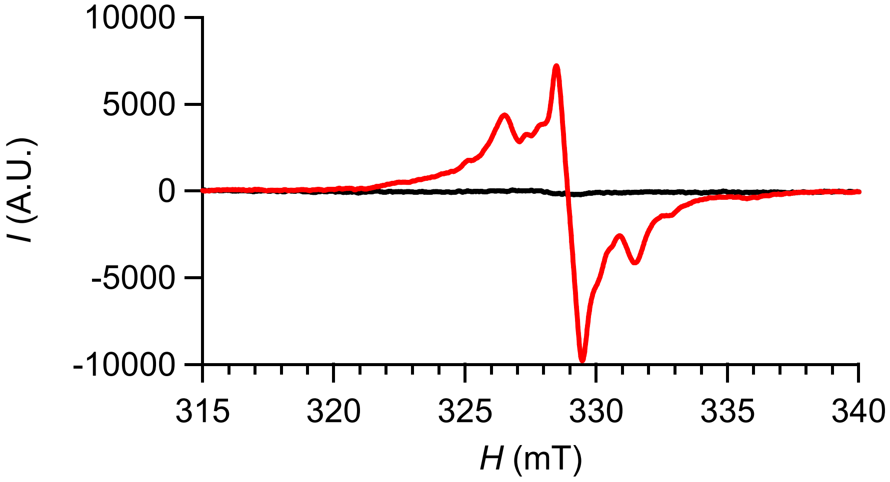

Figure S11 (Continued).

(**E**) Anisotropy in the electron spin resonance spectra for BPY[Ni(dmit)$_2$]$_6$·3CH$_3$CN (single crystal) observed under UV (250–450 nm; 6.7 W cm^{-2}) irradiation at 123 K. The observed small anisotropy is consistent with the crystal structure and the localized picture of the π-spins on the BPY cations, which implies that the signal originates from the spins on the BPY cations in BPY[Ni(dmit)$_2$]$_6$·3CH$_3$CN. The crystal was rotated by ~90° around the *a*-axis so that magnetic field (*H*) was // *b*-axis (**red**) or // *c*-axis (**blue**). The UV light was incident on the *ab*-plane (**red**) or on the *ac*-plane (**blue**).

(**F**) Electron spin resonance spectra for BPY·Br$_2$ (single crystal) observed under dark (**black**) and UV (250–450 nm; 6.7 W cm^{-2}) irradiation (**red**) at 123 K. The apparent close similarity of the lineshape between the **red** spectrum in this figure (BPY·Br$_2$) and that in the UV-irradiated BPY[Ni(dmit)$_2$]$_6$·3CH$_3$CN (the **red** spectrum in **Figure S11C**) indicates that the observed peaks in the latter spectra (the **red** spectrum in **Figure S11C**) can be assigned to the spins on the BPY cations.

G

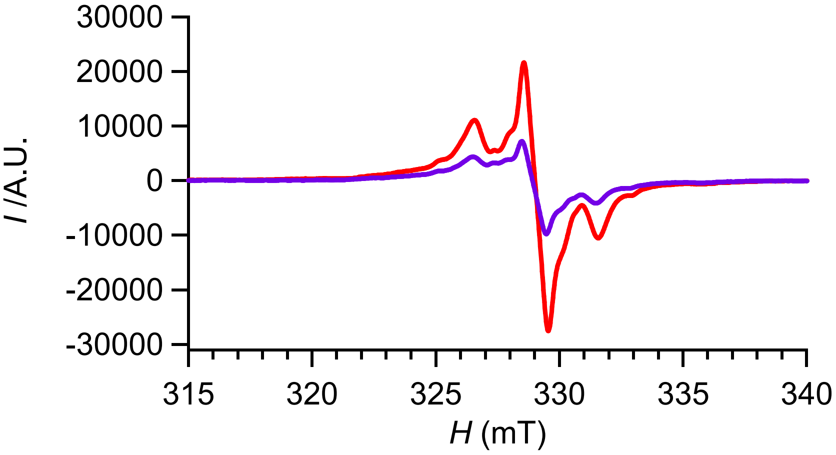

H

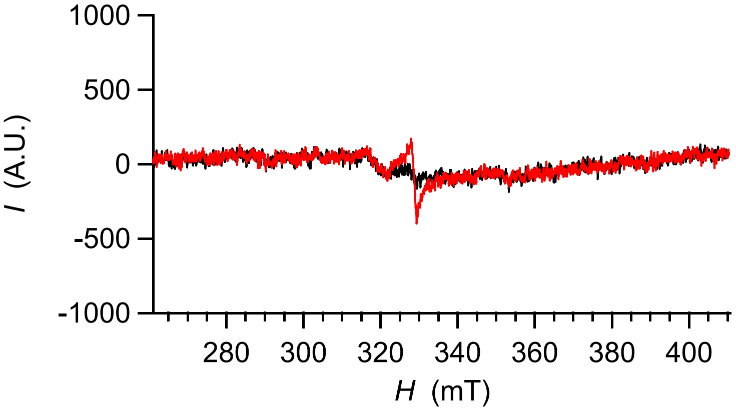

Figure S11 (Continued).

(**G**) Comparison of the electron spin resonance spectra for BPY·Br_2 (single crystal; **purple**; the **red** spectrum in **Figure S11F**) and BPY[Ni(dmit)$_2$]$_6$·3CH_3CN (single crystal; **red**; the **red** spectrum in **Figure S11C**) showing that they both originate from the spins on the BPY cations with similar electronic states. Both spectra were observed under UV (250–450 nm; 6.7 W cm^{-2}) irradiation at 123 K. The spectra are almost identical, except for the intensities. The absolute intensities are governed by the dimensions of the crystals utilized in the measurements and are thus extrinsic.

(**H**) Electron spin resonance spectra for BPY[Ni(dmit)$_2$]$_6$·3CH_3CN (single crystal) observed under dark conditions (**black**) and under a selected range of UV (240–300 nm; 10.5 mW cm^{-2}) irradiation (**red**) at 123 K. As shown below, the spectral simulation (**Figure S11I** and **Table S4C**) indicates that the observed signal under UV irradiation can be assigned to the spins on the BPY cations. Magnetic field (*H*) // *b*-axis. UV was incident on the *ab*-plane.

I

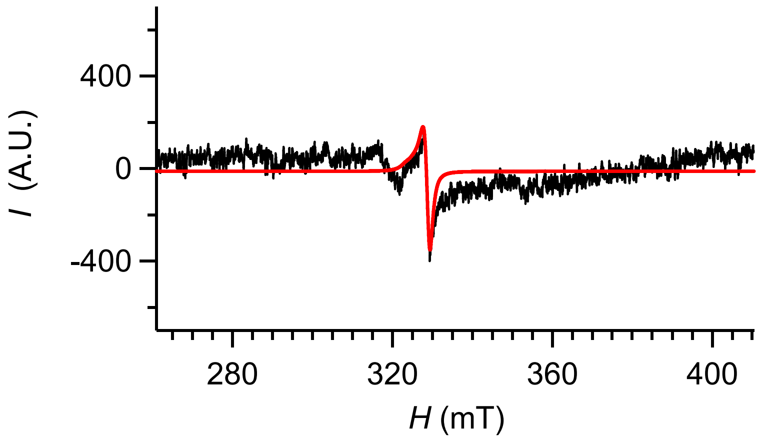

J

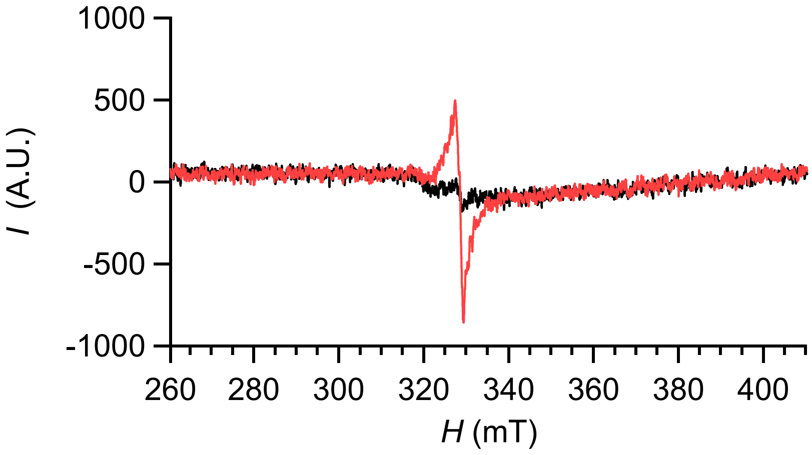

Figure S11 (Continued).

(**I**) Electron spin resonance spectrum for BPY[Ni(dmit)$_2$]$_6$·3CH$_3$CN (single crystal) observed under a selected range of UV (240–300 nm; 10.5 mW cm^{-2}) irradiation (**black**) at 123 K and simulated spectrum (**red**). The moderate agreement between the two spectra demonstrates that the observed signal can be assigned to the spins on the BPY cations. Magnetic field (*H*) // *b*-axis. The UV light was incident on the *ab*-plane. The spectrum in **black** is the same as that in **red** in **Figure S11H**.

(**J**) Electron spin resonance spectra for BPY[Ni(dmit)$_2$]$_6$·3CH$_3$CN (single crystal) observed under dark (**black**) and under a selected range of UV (300-400 nm; 36.7 mW cm^{-2}) irradiation (**red**) at 123 K. As shown below, the spectral simulation (**Figure S11K** and **Table S4D**) indicates that the observed signal under UV irradiation can be assigned to the spins on the BPY cations. Magnetic field (*H*) // *b*-axis. The UV light was incident on the *ab*-plane.

K

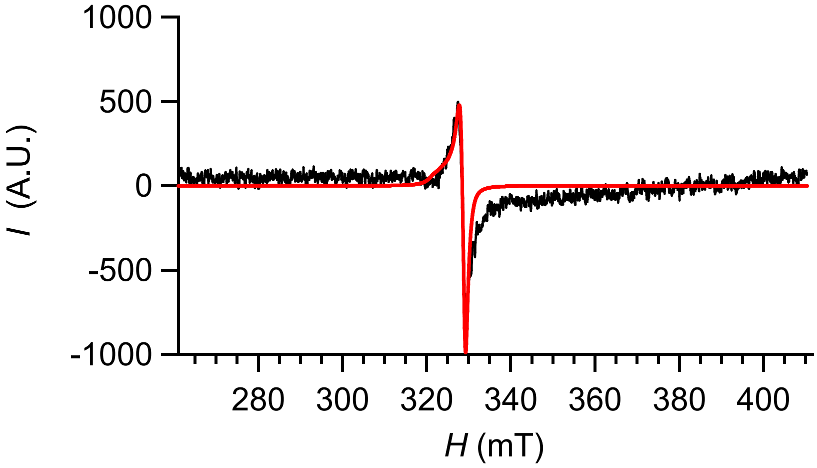

Figure S11 (Continued).

(**K**) Electron spin resonance spectrum for BPY[Ni(dmit)$_2$]$_6$·3CH$_3$CN (single crystal) observed under a selected range of UV (300–400 nm; 36.7 mW cm^{-2}) irradiation (**black**) at 123 K and simulated spectrum (**red**). The agreement between the two spectra demonstrates that the observed signal can be assigned to the spins on the BPY cations. Magnetic field (*H*) // *b*-axis. The UV light was incident on the *ab*-plane. The spectrum in **black** is the same as that in **red** in **Figure S11J**.

L

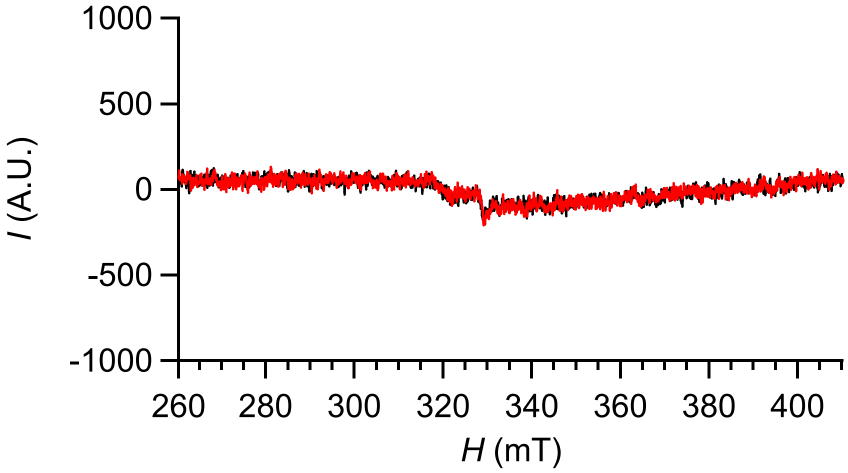

Figure S11 (Continued).

(**L**) Electron spin resonance (ESR) spectra for BPY[Ni(dmit)$_2$]$_6$·3CH$_3$CN (single crystal) observed under dark (**black**) and a selected range of visible light (400-700 nm; 242.5 mW cm^{-2}) irradiation (**red**) at 123 K. The two spectra are identical, indicating that visible light irradiation does not change the ESR spectrum. Magnetic field (*H*) // *b*-axis. The visible light was incident on the *ab*-plane.

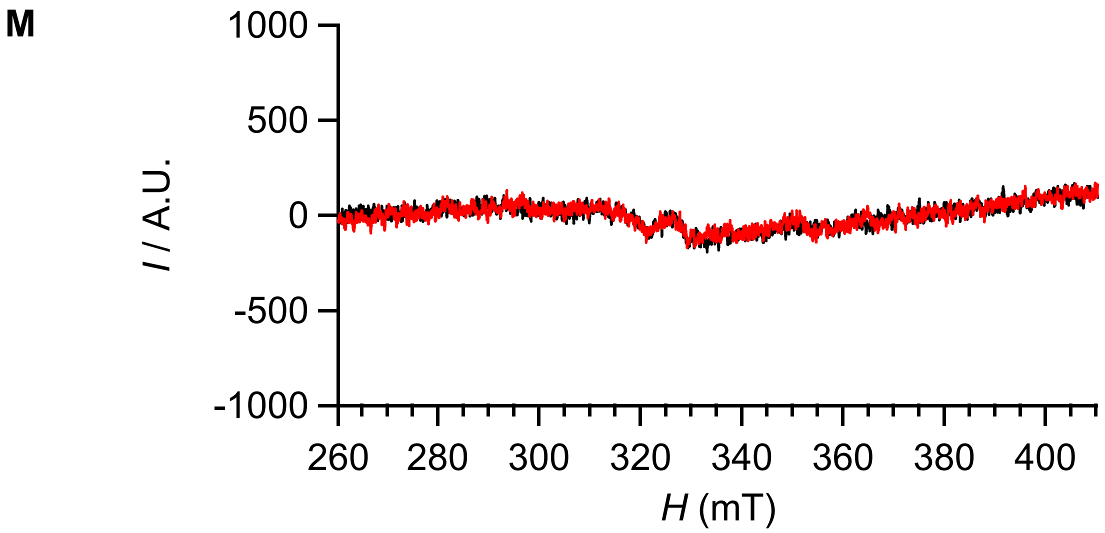

Figure S11 (Continued).

(**M**) Electron spin resonance (ESR) spectra for BPY[Ni(dmit)$_2$]$_6$·3CH$_3$CN (single crystal) observed under dark (**black**) and a selected range of IR light (700–4000 nm; 13.5 mW cm^{-2}) irradiation (**red**) at 123 K. The two spectra are identical, indicating that IR light irradiation does not change the ESR spectrum. Magnetic field (*H*) // *b*-axis. The IR light was incident on the *ab*-plane.

Table S4.

Parameters used in the spectral simulation for BPY[Ni(dmit)$_2$]$_6$·3CH$_3$CN measured (**A**) under UV (375 ± 5 nm; 14.4 mW cm^{-2}) irradiation (shown in **Figure S11B**),a) (**B**) under UV (250–450 nm; 6.7 W cm^{-2}) irradiation (shown in **Figures S11C** and **S11D**),a) (**C**) under UV (240–300 nm; 10.5 mW cm^{-2}) irradiation (shown in **Figures S11H** and **S11I**),a) and (**D**) under UV (300–400 nm; 36.7 mW cm^{-2}) irradiation (shown in **Figures S11J** and **S11K**).a)

A

Oscillator # b)	#1	#2
I_{rel}(%)	87.5	12.5
I	1 (^{14}N)	0 (^{12}C)
g_x	2.0339	2.0035
g_y	2.0029	2.0035
g_z	2.0029	2.0035
A_x (mT)	2.0000	NA
A_y (mT)	0.3000	NA
A_z (mT)	0.3000	NA
Γ_x (mT)	2.0000	2.0000
Γ_y (mT)	0.8000	2.0000
Γ_z (mT)	0.8000	2.0000
Lorentzian/Gaussian	100/0	0/100

B

Oscillator # b)	#1	#2
I_{rel} (%)	66.7	33.3
I	1 (^{14}N)	0 (^{12}C)
g_x	2.0019	2.0029
g_y	2.0029	2.0029
g_z	2.0029	2.0029
A_x (mT)	2.0000	NA
A_y (mT)	0.1000	NA
A_z (mT)	0.1000	NA
Γ_x (mT)	0.5000	1.1000
Γ_y (mT)	0.8000	1.1000
Γ_z (mT)	0.8000	1.1000
Lorentzian/Gaussian	100/0	0/100

C

Oscillator #b)	#1	#2
I_{rel} (%)	90	10
I	1 (^{14}N)	0 (^{12}C)
g_x	2.0239	2.0035
g_y	2.0029	2.0035
g_z	2.0029	2.0035
A_x (mT)	2.0000	NA
A_y (mT)	0.3000	NA
A_z (mT)	0.3000	NA
Γ_x (mT)	2.0000	2.0000
Γ_y (mT)	1.0000	2.0000
Γ_z (mT)	1.0000	2.0000
Lorentzian/Gaussian	100/0	0/100

D

Oscillator #b)	#1	#2
I_{rel} (%)	87.5	12.5
I	1 (^{14}N)	0 (^{12}C)
g_x	2.0339	2.0035
g_y	2.0029	2.0035
g_z	2.0029	2.0035
A_x (mT)	2.0000	NA
A_y (mT)	0.3000	NA
A_z (mT)	0.3000	NA
Γ_x (mT)	2.0000	2.0000
Γ_y (mT)	0.8000	2.0000
Γ_z (mT)	0.8000	2.0000
Lorentzian/Gaussian	100/0	0/100

a) I_{rel}, I, g_i, A_i, and Γ_i ($i = x, y, z$) are the relative intensity, nuclear spin, g-value, hyperfine coupling constant, and linewidth in the i direction, respectively. b) #1 and #2 designate the serial numbers of the oscillators required to reproduce the observed spectra. This does not mean that there are such numbers of independent spins in the sample.

§5. Photoconduction

Table S5.

Parameters obtained from the curve-fitting analysis of photoconduction data shown in **Figure 5B** using equation (1) (n = 0–3).

T/K	c_0	c_1 /W^{-1}cm^2	c_2 /W^{-2}cm^4	c_3 /W^{-3}cm^6
293	1.00397	0.109984	0	0
280	1.00178	0.119311	0	0
260	1.00055	0.224866	0	0
240	1.00205	0.219069	0	0
220	1.00017	0.21071	0	0.00035757
200	0.997803	0.364501	0	0.0058462
180	0.992735	0.46211	0	0.017219
160	0.971355	0.80202	0	0.049091
140	0.99249	1.6299	0	0.094575
120	0.960041	2.2253	-0.061418	0.35557
100	0.95863	1.9526	1.3224	0.79088
81	0.96000	5.3579	0.6376	9.6635

T/K	σ_{dark} [a] /10^{-5} S	σ_{heat} [a] /10^{-5} S	σ_{opt} [a] /10^{-5} S
293	466.81	79.628	0
280	270.61	50.077	0
260	429.81	149.898	0
240	293.41	99.692	0
220	215.50	70.428	0.287506
200	156.36	88.393	3.41052
180	89.548	64.182	5.75306
160	45.012	55.992	8.24449
140	17.003	42.984	5.99991
120	5.4444	18.791	6.41853
100	1.3960	4.228	8.56035
81	0.3794	3.152	14.2594

[a] Conductivities are shown as surface conductivities in the unit of Siemens (S), as it is independent of the penetration depth of UV irradiation.

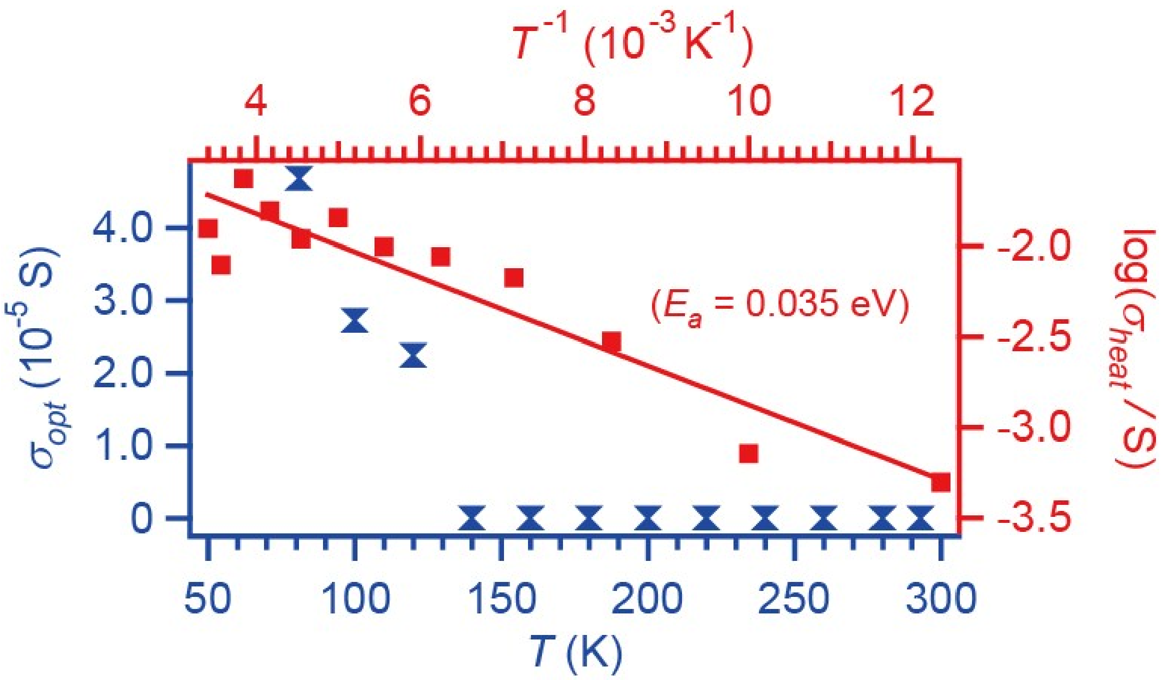

Figure S12. σ_{opt} (S) *vs* T (K) (**blue**) and the Arrhenius plot of σ_{heat} (**red**). Different data from **Figure 5D** under irradiation of $I = 1.551$ (W cm^{-2}). It should be noted here that the temperature of an anomaly in E_a ($T^* \sim 200$ K; $10^3 T^{*-1} \sim 5$) derived from the analysis (log(σ_{heat}) *vs.* T^{-1} in **Figure S12**) coincides with that directly observed ($10^3 T^{-1} \sim 5$) in **Figure 2B**. In addition, among different samples, the temperature where σ_{opt} begins to rapidly increase (~150–200 K) also approximately coincides with T^*, the reason for which remains to be clarified in further studies.

Measurements and analysis of purely optical effects in conduction

Generally, the temperature-dependence of the resistivity without irradiation is measured by slowly changing the temperature. However, the temperature dependence of the resistivity under irradiation, *i.e.*, photoconductivity, could not be measured in the same way. The temperature differences between the sample and the thermometer were large and irreproducible. This situation was independent of the rate of temperature variation or the waiting time, which made it difficult to correct the temperature. The problem was solved by the repeated resistivity measurements (using a standard four-probe method) at a constant temperature and constant light intensity.

An additional problem is that one could not know the exact portion of irradiation in the samples, which makes it difficult to estimate the absolute values of the photoconductivity and exact ratios between the dark- and photo-conductivities. To distinguish these thermal effects from net optical effects, we recently found a general method based on the dependence of the photocurrent on the light intensity.[S9] This method is applied in the present work.

At a constant temperature T,[S10] the observed dependence of the photoconductivity $\sigma(I,T)$ on the light intensity I was well reproduced by a polynomial of I,

$$\sigma(I,T) = \sum_{n=0} c_n I^n \sigma_{dark}(T) \tag{1}$$

where c_n (n = 0, 1, 2, …) represents experimentally-determined constants (fitting parameters dependent on T), and c_0 should be unity if the model is consistent.

The basis of eq 1 is shown as follows. The photoconductivity at T under irradiation I can be divided into three terms from different origins.

$$\sigma(I,T) = \sigma_{dark}(T) + \sigma_{heat}(I) + \sigma_{miscel} \tag{S1}$$

where $\sigma_{dark}(T)$, $\sigma_{heat}(I)$, and σ_{miscel} designate the dark conductivity at T, conductivity change from the heat involved with irradiation I, and remaining contributions from miscellaneous origins, respectively. The contribution to conduction from photoexcited carriers is included in σ_{miscel}, which is a function of T and I in general.

$\sigma_{dark}(T)$ is directly measured under dark conditions. At a given T, *i.e.*, at a constant temperature, $\sigma_{dark}(T)$ is a constant and corresponds to the first term in eq 1.

$\sigma_{heat}(I)$ is described as follows.

$$\sigma_{heat} = \frac{d\sigma_{dark}}{dT}\Delta T \tag{S2}$$

where ΔT is the difference in T between the surroundings and sample under irradiation.

ΔT is formulated based on two assumptions: the heat Q from the light is proportional to the light intensity I, and the heat capacity $C(T)$ of the sample is proportional to T^3 considering the contribution from phonons (Debye model of the lattice heat capacity). The contribution to the heat capacity from electrons can be ignored in the temperature range of the measurements (77 K < T < 300 K). Therefore,

$$Q = AI \tag{S3}$$

$$C(T) = \alpha T^3 \tag{S4}$$

where A and α are the proportional constants, respectively. Even if A is a function of T instead of a constant, the discussion below is still valid with only modification on the T^{-3} dependence in eqs S5-S8. Thus

$$\Delta T = \frac{Q}{C(T)} = \frac{AI}{\alpha T^3} = \frac{BI}{T^3} \left(B \equiv \frac{A}{\alpha}; constant\right) \tag{S5}$$

By substituting eq S5 into eq S2,

$$\sigma_{heat} = \frac{d\sigma_{dark}}{dT}\Delta T = \frac{d\sigma_{dark}}{dT}\frac{BI}{T^3} \tag{S6}$$

Therefore, under a given T, *i.e.*, at a constant temperature T_0, σ_{heat} in eq S6 is described as

$$\sigma_{heat} = (constant) \times I \tag{S7}$$

where

$$(constant) = \left.\frac{d\sigma_{dark}}{dT}\frac{B}{T^3}\right|_{T = T_0} \tag{S8}$$

Thus, σ_{heat} in eq S7 corresponds to the second term, which is proportional to I in eq 1.

The formulation of σ_{miscel} is dependent on each case and should vary with respect to the photoconduction mechanism. However, under a given T and I, *i.e.*, at a constant temperature and constant light intensity, different formulas of σ_{miscel} would give a practically identical value of σ_{miscel} in principle, if eq 1 well reproduces the observed behavior (Fig. S13). Therefore, one can analyze the photoconduction using eq 1 without knowing the details of the photoconduction mechanism. Similarly, the arbitrariness in fitting analysis does not affect the discussion and conclusion on σ_{heat} and σ_{miscel}. The obtained parameters are summarized in **Table S5**, which shows that σ_{opt} is non-zero and rapidly increases at $T \leq 220$ K.

$$\sigma_{opt} \equiv \sum_{n \geq 2} c_n I^n \sigma_{dark}$$

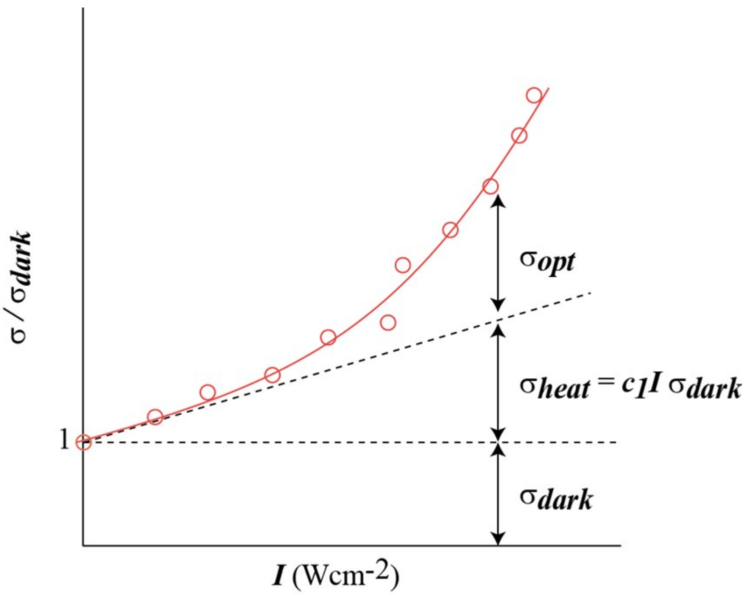

Figure S13. Schematic description for analysis of photoconduction using eq 1.

§6. References and notes

S1 For the occupied valence atomic orbitals of the elements from H (hydrogen) to U (uranium), the CRMM set provides the exponents of the STO's taken from the Hartree-Fock calculations by Clementi and Roetti[S11] and by McLean and McLean.[S12] The H_{ii} (*i.e.*, VSIP = valence-state ionization potential [eV]) values of these orbitals were approximated by their orbital energies obtained from the Hartree-Fock calculations. For the unoccupied valence atomic orbitals, for which the Hartree-Fock calculations do not provide any information, their parameters were taken from the ADF set. For the valence atomic orbitals of the elements from H to U, the ADF basis set provides the exponents of the STO's used in the Amsterdam Density Functional (ADF) program package.[S13] The H_{ii} values of these orbitals were approximated by their orbital energies calculated from ADF calculations for atoms. The Collected set provides a collection of the atomic orbital parameters used for extended Hückel tight-binding (EHTB) calculations over the years at R. Hoffmann's laboratory in Department of Chemistry, North Carolina State University, Raleigh, North Carolina, USA and related researchers. For details of the atomic orbital parameters and basis sets utilized in CAESAR, see the PDF manual of CAESAR package (pp. 85-87 in Chapter 5) available from http://www.primec.com/publications.htm for free.

S2 Naito, T.; Karasudani, T.; Mori, S.; Ohara, K.; Konishi, K.; Takano, T.; Takahashi, Y.; Inabe, T.; Nishihara, S.; Inoue, K. *J. Am. Chem. Soc.* **2012**, *134*, 18656-18666.

S3 Gaussian 09, Revision C.01, Frisch, M. J.; Trucks, G. W.; Schlegel, H. B.; Scuseria, G. E.; Robb, M. A.; Cheeseman, J. R.; Scalmani, G.; Barone, V.; Mennucci, B.; Petersson, G. A.; Nakatsuji, H.; Caricato, M.; Li, X.; Hratchian, H. P.; Izmaylov, A. F.; Bloino, J.; Zheng, G.; Sonnenberg, J. L.; Hada, M.; Ehara, M.; Toyota, K.; Fukuda, R.; Hasegawa, J.; Ishida, M.; Nakajima, T.; Honda, Y.; Kitao, O.; Nakai, H.; Vreven, T.; Montgomery, Jr., J. A.; Peralta, J. E.; Ogliaro, F.; Bearpark, M.; Heyd, J. J.; Brothers, E.; Kudin, K. N.; Staroverov, V. N.; Kobayashi, R.; Normand, J.; Raghavachari, K.; Rendell, A.; Burant, J. C.; Iyengar, S. S.; Tomasi, J.; Cossi, M.; Rega, N.; Millam, J. M.; Klene, M.; Knox, J. E.; Cross, J. B.; Bakken, V.; Adamo, C.; Jaramillo, J.; Gomperts, R.; Stratmann, R. E.; Yazyev, O.; Austin, A. J.; Cammi, R.; Pomelli, C.; Ochterski, J. W.; Martin, R. L.; Morokuma, K.; Zakrzewski, V. G.; Voth, G. A.; Salvador, P.; Dannenberg, J. J.; Dapprich, S.; Daniels, A. D.; Farkas, O.; Foresman, J. B.; Ortiz, J. V.; Cioslowski, J.; Fox, D. J. Gaussian, Inc., Wallingford CT, 2009.

S4 GaussView, Version 5, R. Dennington, T. Keith, J. Millam, *Semichem Inc.*, Shawnee Mission KS, 2009.

S5 Naito, T.; Karasudani, T.; Ohara, K.; Takano, T.; Takahashi, Y.; Inabe, T.; Furukawa, K.; Nakamura, T. *Avd. Mater.* **2012**, *24*, 6153-6157.

S6 Noma, H.; Ohara, K.; Naito, T. *Inorganics* **2016**, *4*, 7.

S7 Naito, T.; Inabe, T.; Niimi, H.; Asakura, K. *Adv. Mater.* **2004**, *16*, 1786-1790.

S8 Naito, T.; Sugawara, H.; Inabe, T.; Kitajima, Y.; Miyamoto, T.; Niimi, H.; Asakura, K. *Adv. Func. Mater.* **2007**, *17*, 1663-1670.

S9 N. Nagayama, T. Yamamoto, T. Naito, *CheM* **2015**, 74-80 (2015).

http://ccaasmag.org/chem_2012/vol2/Naito-photoconduction.pdf#search=%27N.+Nagayama%2C+T.+Yamamoto%2C+T.+Naito%2C+CheM+2015%2C+7480+%282015%29%27

S10 The temperature *T* designates that of surroundings, which could be different from an effective temperature of sample under irradiation.

S11 Clementi, E.; Roetti, C. *Atomic Data Nuclear Data Tables*, **1974**, *14*, 177.

S12 McLean, A. D.; McLean, R. S. *Atomic Data Nuclear Data Tables*, **1981**, *26*, 197.

S13 (a) ADF Release 1.1.3, Department of Chemistry, Vrije Universiteit, Amsterdam. (b) Baerends, E. J.; Ellis, D. E.; Ros, P., *Chem. Phys.*, **1973**, *2*, 41. (c) te Velde, G.; Baerends, E. J., *J. Comp. Phys.*, **1992**, *99*, 84.